

OTELO Survey: Deep BVRI broadband photometry of the Groth strip

II. Properties of X-ray Emitters

M. Pović

Instituto de Astrofísica de Canarias, 38205 La Laguna, Spain

mpovic@iac.es

M. Sánchez-Portal

Herschel Science Centre, ESAC/INSA, P.O. Box 78, 28691 Villanueva de la Cañada, Madrid, Spain

miguel.sanchez@sciops.esa.int

A. M. Pérez García

Instituto de Astrofísica de Canarias, 38205 La Laguna, Spain

A. Bongiovanni

Instituto de Astrofísica de Canarias, 38205 La Laguna, Spain

J. Cepa¹

Departamento de Astrofísica, Universidad de La Laguna, 38205 La Laguna, Spain

J.A. Acosta-Pulido

Instituto de Astrofísica de Canarias, 38205 La Laguna, Spain

E. Alfaro

Instituto de Astrofísica de Andalucía-CSIC, Granada, Spain

H. Castañeda

Instituto de Astrofísica de Canarias, 38205 La Laguna, Spain

M. Fernández Lorenzo

Instituto de Astrofísica de Canarias, 38205 La Laguna, Spain

J. Gallego

Departamento de Astrofísica y CC. de la Atmósfera, Universidad Complutense de Madrid, Madrid, Spain

J. I. González-Serrano

Instituto de Física de Cantabria, CSIC-Universidad de Cantabria, Santander, Spain

J. J. González

Instituto de Astronomía UNAM, México D.F, México

M. A. Lara-López

Instituto de Astrofísica de Canarias, 38205 La Laguna, Spain

ABSTRACT

The Groth field is one of the sky regions that will be targeted by the OTELO (OSIRIS Tunable Filter Emission Line Object) survey in the optical 820 nm and 920 nm atmospheric windows. This field has been observed by AEGIS (All-wavelength Extended Groth strip International Survey) covering the full spectral range, from X-rays to radio waves. *Chandra* X-ray data with total exposure time of 200ksec are analyzed and combined with optical broadband data of the Groth field in order to study a set of structural parameters of the X-ray emitters and its relation with X-ray properties. We processed the raw, public X-ray data using the *Chandra* Interactive Analysis of Observations and determined and analyzed different structural parameters in order to produce a morphological classification of X-ray sources. Finally, we analyzed the angular clustering of these sources using 2-point correlation functions. We present a catalog of 340 X-ray emitters with optical counterpart. We obtained the number counts and compared them with AEGIS data. Objects have been classified by nuclear type using a diagnostic diagram relating X-ray-to-optical ratio (X/O) to hardness ratio (HR). Also, we combined structural parameters with other X-ray and optical properties, and found for the first time an anticorrelation between the X/O ratio and the Abraham concentration index which might suggest that early type galaxies have lower Eddington rates than those of late type galaxies. A significant positive angular clustering was obtained from a preliminary analysis of 4 subsamples of the X-ray sources catalog. The clustering signal of the optically extended counterparts is similar to that of strongly clustered populations like red and very red galaxies, suggesting that the environment plays an important role in AGN phenomena.

Subject headings: Galaxies: active — X-rays: galaxies

1. Introduction

The OTELO project (Cepa et al. 2005, 2008) is a flux-limited survey of emission-line objects in large and perfectly defined volumes of the Universe. The OTELO survey, more than one magnitude deeper than other emission line surveys, includes a wide variety of astronomical sources: star-forming galaxies, starburst galaxies, emission-line ellipticals, AGNs, QSOs, Ly α emitters, peculiar stars, etc. With these data, a number of scientific problems will be addressed,

including: star formation rates (SFR) and metallicity evolution of galaxies; AGN and QSO evolution. Deep imaging programs such as several VLT surveys for GOODS (Dickinson et al. 2004), COSMOS (Capak et al. 2007) and SXDS (Furusawa et al. 2008) fields will serve as preparatory work for OTELO. Likewise, we have performed a deep BVRI broadband survey in one of the fields of the Groth strip selected for the OTELO survey (Cepa et al. 2008).

In the present work, data from this broad band survey is combined with other wavelength data

¹Instituto de Astrofísica de Canarias, 38205 La Laguna, Spain

for achieving several objectives of the OTELO project. Specifically, the matching of these optical data with X-ray allows successfully tackling the study of the AGN population as shown in Barcons et al. (2007), Georgakakis et al. (2006), and Steffen et al. (2006). Optical imaging surveys allow a morphological classification of all sufficiently resolved sources. This is essential to reveal the nature of AGN host galaxies (e.g. Hasan 2007; Fiore et al. 2001), although the morphological classification becomes difficult at high redshift, due to the reduced resolution of images. Several works (Graham et al. 2001b; Ferrarese & Merrit 2000; Gebhardt et al. 2000) have shown that the AGNs are directly related with some host galaxy properties, particularly with their bulges. Kauffmann et al. (2003) have pointed out that the AGNs in the local universe are hosted predominantly in bulge-dominated galaxies. More recently, Hasan (2007) using HST and *Chandra* data of the GOODS South field has found that the most moderate luminosity AGNs hosts are bulge-dominated in the redshift range $z \sim 0.4-1.3$. A tight correlation between black hole mass and the bulge dispersion velocity has been well established (Ferrarese & Merrit 2000; Gebhardt et al. 2000), as well as with the concentration of bulges (Graham et al. 2001b).

On the other hand, deep X-ray extragalactic surveys are extremely useful tools to investigate the time evolution of the population of active galactic nuclei (AGN) and to shed light on their triggering mechanisms. The exceptional effectiveness at finding AGN arises largely because X-ray selection has reduced absorption bias, minimal dilution by host-galaxy starlight and allows efficient optical spectroscopic follow-ups of high probability AGN candidates with faint optical counterparts. The *Chandra* and *XMM-Newton* observatories have revolutionized this field of research, generating the most sensitive X-ray surveys ever performed. In fact, deep surveys produced by these observatories have increased the resolved fraction of the cosmic X-ray background (CXRB) to about 90% in the 0.5–2 keV range. A large part of the detected X-ray sources are AGN ($\leq 70\%$), although X-ray emitters include a mix of different types of objects such as galaxy clusters and stars. On the other hand, these powerful observatories make it possible to access

the hard (2–10 keV) range, allowing to directly probe the AGN activity not contaminated by star formation processes. Moreover, hard X-ray surveys are capable to detect all but the most absorbed (Compton thick) sources. Therefore, they provide the most complete and unbiased samples of AGNs (Mushotzky 2004; Brandt & Hasinger 2005). Number counts relations have now been determined (e.g. Cappelluti et al. 2007) although with some evidence for field-to-field variations. Such variations are expected at some level owing to "cosmic statistics" associated with large-scale structures and clustering features that have been detected in the X-ray sky (Barger et al. 2003; Yang et al. 2003; Gilli et al. 2003, 2005).

In this paper we present the analysis of public, deep (200 ksec) *Chandra*/ACIS observations of three fields comprising the original Groth-Westphal strip (GWS), gathered from the *Chandra* Data Archive, and combined with optical BVRI data from our broadband survey carried out with the 4.2m William-Herschel Telescope (WHT) at La Palma (see Cepa et al. 2008, for a detailed description). We have tried to implement an innovative approach to the optical study of X-ray emitters by investigating correlations between broadband optical and X-ray parameters, specifically the X-ray-to-optical ratio and hardness ratios, and optical structural parameters that provide information about the host galaxy morphology and populations, like asymmetry and concentration indexes and optical colors.

This paper is structured as follows: in Section 2, we describe the observational data, including X-ray data processing and source detection, as well as optical broadband data and the selection of the sample of X-ray sources with optical counterparts. Section 3 reviews the X-ray properties of the galaxy sample, the procedures for computing optical structural parameters, as well as the morphological analysis carried out. The reliability of different structural parameters used in morphological classification is also discussed. Section 4 presents the nuclear type classification, the relationship between X-ray and optical structural properties, and the comparison with results from the literature. The catalog of X-ray emitters with optical counterparts and their morphological classification is presented in the electronic edition. Finally, in Section 5 we present the results of the

clustering analysis (based on the angular correlation function formalism) applied on 4 selected subsamples of the X-ray catalog.

2. Observational data

2.1. X-ray data

2.1.1. Observations and data processing

Chandra has observed three consecutive fields centered at the original HST Groth-Westphal strip (GWS) using the ACIS-I instrument. All datasets have been gathered from the *Chandra* Data Archive (<http://asc.harvard.edu/cda/>) using the Chaser tool. PI of all the retrieved *Chandra* observations is K. Nandra. Total exposure time in each field is about 200 ksec. The total field size of ACIS-I chips 0, 1, 2 & 3 is $16.9' \times 16.9'$ (ACIS-S chips 2 & 3 were also used, but their FOVs do not overlap with our optical data and therefore were not used). The FAINT and VFAINT telemetry modes have been used, with telemetry saturation rates of 170 and 67 events/s, respectively. Due to the lack of bright sources within the fields, we assume that there are no pile-up effects in any observation. Table 1 summarizes the main characteristics of the *Chandra* observations.

We processed the data Using the *Chandra* Interactive Analysis of Observations (CIAO) (<http://cxc.harvard.edu/ciao/>), v4.0 and Calibration Data Base (CALDB) v3.4.0. Standard reduction procedures have been applied, as described in the CIAO Science Threads to produce new level 2 event files. The output level 2 event files have been restricted to the 0.5–8 keV range to avoid high background spectral regions. Furthermore, we analyzed the source-free light curves in order to define additional good time intervals (GTI). To this end, we applied the CIAO detection program `celldetect` with a threshold $S/N=3$. The detected sources have been removed upon creation of the time-binned light curves, that have been then used for the computation of the GTIs. A $\pm 3\sigma$ rejection criterion has been applied to remove high background intervals. After filtering for the additional GTIs, the level 2 event files belonging to the same target were co-added. To this end, we first improved the absolute astrometry (the overall 90% uncertainty circle of *Chandra* X-ray absolute position has a radius of 0.6 arcsec)

Table 1: *Chandra* observations log for the three pointings of the GWS field. Col. (1): observation number; Col. (2,3): RA and DEC (J2000); Col. (4): Standard Data Processing (SDP) version; Col. (5): Observation format in the Time exposure mode; Col. (6): Net exposure time (Sum of Good Time Intervals, GTI) (ksec)

Obs (1)	RA (2)	DEC (3)	SDP (4)	Mode (5)	GTI (6)
5853	14:15:22.5	+52:08:26.4	7.6.7.1	VFAINT	42.4
5854			7.6.7.1	VFAINT	50.2
6222			7.6.7.1	VFAINT	35.2
6223			7.6.7.1	VFAINT	49
6366			7.6.7.1	VFAINT	15.96
7187			7.6.7.1	VFAINT	8
5851	14:16:24.5	+52:20:02.59	7.6.7.1	VFAINT	36
5852			7.6.4	VFAINT	11.95
6220			7.6.7.1	VFAINT	36
6221			7.6.7.1	VFAINT	3.8
6391			7.6.7.1	VFAINT	9.4
7169			7.6.4.1	VFAINT	18.2
7181			7.6.7.1	VFAINT	8
7188			7.6.4.1	VFAINT	4.2
7236			7.6.4	VFAINT	18.8
7237			7.6.4.1	VFAINT	17.2
7238			7.6.4	VFAINT	9.6
7239			7.6.4.1	VFAINT	16.2
3305	14:17:43.0	+52:28:25.2	6.8.0	FAINT	27.6
4357			6.9.0	FAINT	79.8
4365			6.9.0	FAINT	58.2

applying corrections for translation, scale and rotation to the world coordinate system (WCS) of each data file, by comparing two sets of source lists from the same sky region. Average positional accuracy improvement is 6.3% with respect to the original astrometry provided by the spacecraft attitude files. Once we have improved the astrometry, the event files have been merged.

The output merged files have been filtered to create event files for several energy bands: full (0.5–7 keV), soft (0.5–2 keV), hard (2–7 keV) hard2 (2–4.5 keV) and vhard (4–7 keV). Unbinned effective exposure maps at a single energy, representative of each band, were created at 2.5 keV (full), 1 keV (soft), 4 keV (hard), 3 keV (hard2) and 5.5 keV (vhard). Resulting maps have units of time \times effective area, i.e. $\text{s cm}^2 \text{ counts photon}^{-1}$.

2.1.2. Source detection

We applied the CIAO `wavdetect` Mexican-Hat wavelet source detection¹ program to all bands (full, soft, hard, hard2 and vhard) for the three fields. Several wavelet scales have been applied: 1, $\sqrt{2}$, 2, $2\sqrt{2}$, 4, $4\sqrt{2}$, 8, $8\sqrt{2}$ and 16 pixels. Small scales are well suited to the detection of small sources while larger scales are appropriate for more extended sources. Due to the “blank field” nature of the GWS, we do not expect to detect sources at a scale larger than 16 pixels (~ 8 arcsec). For each applied scale, `wtransform` produces a complete set of detections. We set a significance threshold of 2×10^{-7} . Since this `wavdetect` input parameter measures the number of spurious events per pixel, we expect ≈ 0.2 fake detections per detector of 1024×1024 pixels i.e. about 12 spurious sources in the entire catalog (4 detectors \times 5 bands \times 3 fields). The output `wavdetect` detection files are FITS tables containing the position of sources (RA & DEC), count rates in photons $\text{s}^{-1} \text{cm}^{-2}$ and ancillary information. The final X-ray source catalog has been obtained by cross-matching detections in all five bands in order to increase the reliability of detections. Best match is given by a minimum separation of sources around a great circle. We set a maximum search distance of 2 arcsec (see section 2.4). We computed the hardness ratios as follows:

$$HR(\Delta_1 E, \Delta_2 E) = \frac{CR(\Delta_1 E) - CR(\Delta_2 E)}{CR(\Delta_1 E) + CR(\Delta_2 E)} \quad (1)$$

where $\Delta_1 E$ y $\Delta_2 E$ are different energy bands and $CR(\Delta_n E)$ is the count rate in a given energy band. Four hardness ratios have been set in this way: $HR_1 \equiv HR(\text{hard}, \text{soft})$, $HR'_1 \equiv HR(\text{hard2}, \text{soft})$, $HR_2 \equiv HR(\text{very hard}, \text{hard})$ and $HR'_2 \equiv HR(\text{very hard}, \text{hard2})$.

We also computed the energetic fluxes from count rates. To this end, mean photon energies in each band have been calculated assuming a power law spectrum with $\Gamma = 1.5$ (a reasonable assumption after inspecting the hardness ratios diagram and diagnosis grid depicted in Figure 5), redshift $z = 0.5$, galactic absorption $n_H = 1.3 \times 10^{20} \text{cm}^{-2}$

and no intrinsic absorption. We applied the absorption coefficients provided by the `TRANNM` function within the package `PIMMS v3.9b` (Mukai, 1993). The output catalog has 639 unique X-ray emitters (after removing 20 common sources in the field overlapping area). From them, 76 objects are located outside the field covered by optical data. From the total sources, 46% (297) have been detected with a significance $\geq 4\sigma$, 21% (132) above the 3σ significance level and 13% (81) down to 2.5σ level.

The number of sources detected in each band are 490 (full), 465 (soft), 284 (hard), 266 (hard2) and 121 (vhard), with median fluxes of 1.81×10^{-15} , 5.57×10^{-16} , 2.34×10^{-15} , 1.58×10^{-15} and $3.75 \times 10^{-15} \text{erg cm}^{-2} \text{s}^{-1}$, and with limiting fluxes at 3σ level of 4.8×10^{-16} , 1.1×10^{-16} , 2.8×10^{-16} , 1.3×10^{-16} and $7.3 \times 10^{-16} \text{erg cm}^{-2} \text{s}^{-1}$, respectively. Median errors in fluxes (for objects above the 3σ significance level) are 8% in full band, 10% in soft band, 12% in hard band, 14% in hard2 band and 22% in vhard band. There are 16 sources detected only in hard band, 18 in hard2 band and 3 sources are only observed in vhard band. We find an overabundance of soft X-ray sources in our final catalog. There are 103 sources detected only in this band. This effect can be at least partially explained considering the decrease of telescope + ACIS effective area from some 600 cm^2 in the 1–2 keV range (including the 0.5–2 keV band defined as soft), until approximately 200 cm^2 at ~ 6 keV. On the other hand, the total background between 0.5 and 7 keV is around 4 times higher than in the 0.5–2 keV range. The combination of these two factors justifies the high *Chandra*/ACIS source detection efficiency in the soft X-ray band and the mentioned overabundance. The first version of this catalog was presented in Sánchez-Portal et al. (2007).

2.2. Comparison with AEGIS data

The All-wavelength Extended Groth strip International Survey (AEGIS) collaboration has recently made public their data sets, including a catalog of X-ray sources that comprises the observations used within this paper. The complete AEGIS X-ray catalog (Laird et al. 2008) consists of 1325 sources; from these, 471 are located within the area covered by our data (fields EGS-6, 7 and

¹The fact that the PSF of X-ray detectors often has Gaussian-like shape motivates our use of the Marr wavelet, or “Mexican Hat” function.

8 according to their nomenclature). From our 429 sources detected above 3σ significance level, 416 coincide with AEGIS sources using a search radius of 2 arcsec (388 sources if only unique matches are considered). Figure 1 shows a good agreement between the source counts used in this work and those provided by the AEGIS team: median relative deviations of our data with respect to AEGIS are 2% (full band), 0.7% (soft), 5.5% (hard) and 7.8% (vhard).

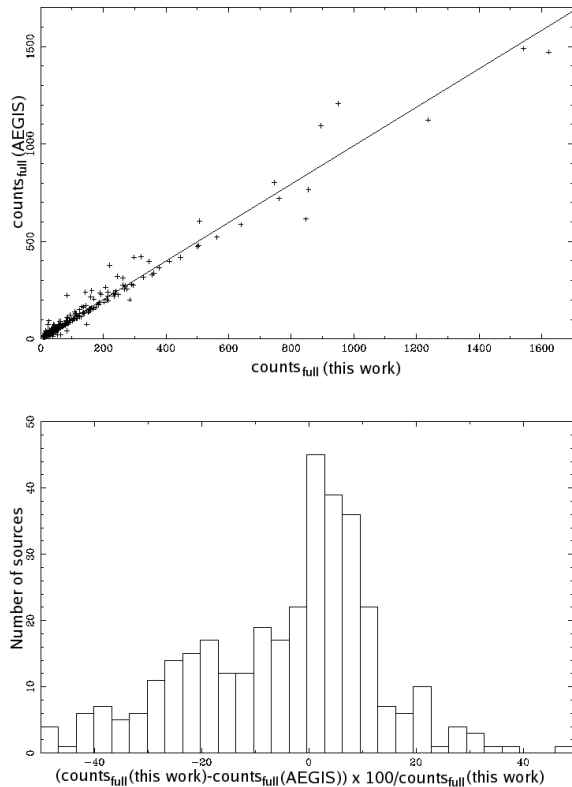


Fig. 1.— Upper panel: full band net counts from this work vs AEGIS net counts. The solid line represents the best linear fit, with a slope of 0.99 and zero point 5.23 counts. Lower panel: histogram of relative deviations of our full band count data with respect to AEGIS. Median deviation is lower than 2%.

2.3. Optical data

We observed three pointings in the direction of the GWS, each of them using the B, V, R, and I broadband filters. The total area covered is 0.18 square degrees. The observations have been car-

ried out using the Prime Focus Imaging Platform (PFIP) at the 4.2m William-Herschel Telescope (WHT) in the Roque de los Muchachos Observatory (La Palma, Canary Islands). This camera has two CCD detectors ($2k \times 4k$), with a total field of view of $16' \times 16'$ and a pixel size of 0.237 arcsec. Several exposures have been performed at each pointing, of 600, 800, 900, or 1000 sec, depending on the filter, with a dithering of 15 arcsec between consecutive exposures in order to allow eliminating cosmic rays and to fill the gap between detectors. Standard reduction procedures have been applied. Resulting limiting magnitudes are 25, 25, 24.5 and 23.5 in B, V, R and I band, respectively. A detailed description of data reduction and optical source detection can be found in Cepa et al. (2008). The optical catalog used in this work contains data for ~ 44000 objects.

2.4. The catalog of optical counterparts

In order to build a sample of X-ray emitters with optical counterparts, we performed cross-matching of the X-ray and optical catalogs using the TOPCAT tool (Taylor 2005), applying a criterion of minimum sky distance along a great circle. X-ray sources located inside the field covered by optical data and their optical counterparts are represented in Figure 2.

We chose a maximum search radius of 2 arcsec after carrying out several tests considering a maximum searching distance of 1 to 5 arcsec with a bin of 0.5 arcsec (Figure 3). As expected, the number of counterparts increases with the maximum search radius, but also the number of multiple matches within the error circle. Setting a search radius of 1 arcsec we minimise the number of multiple cross-matches, but at the cost of losing an outstanding number of potential counterparts. On the other hand, choosing a search radius greater than 2 arcsec produces a large number of multiple matches, increasing the uncertainty in counterpart identification. Therefore, we set a 2 arcsec search radius as an adequate compromise. This practical criterion is consistent with the more rigorous analysis performed below.

We detected 340 optical counterparts of the X-ray sources in at least one optical band. Of them, 322 are detected in the B band, 332 in V, 334 in R and 317 in the I band.

We carried out a quantitative analysis of

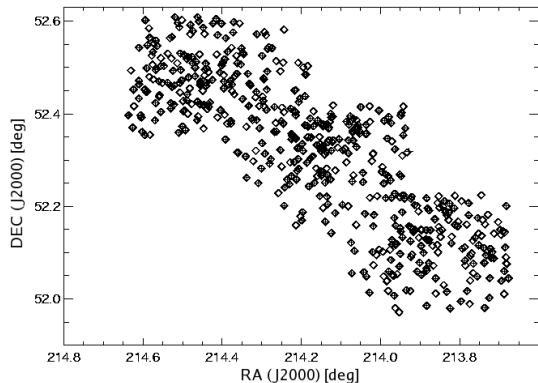


Fig. 2.— X-ray sources (diamonds) and their optical counterparts (filled diamonds) from the cross-match of X-ray and optical catalogs

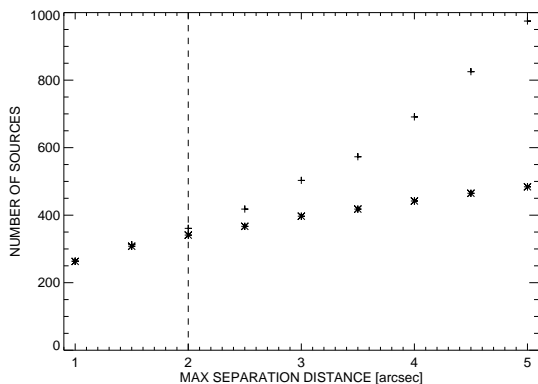


Fig. 3.— Number of optical counterparts as a function of the maximum search radius used for cross-matching. The number of closest sources is represented with stars. Crosses represent the total number of sources found within the search radius. The dashed line marks the adopted separation. The same value was obtained applying the statistical methodology of de Ruiter et al. (1977)

the completeness¹ and reliability² of our cross-matching procedure by applying the methodology of de Ruiter et al. (1977). The separation between sources is defined by the dimensionless variable r as:

¹Fraction of all real associations between the X-ray and optical sources that are indeed classified as identifications.

²Fraction of claimed identifications expected to be true counterparts.

$$r = \left(\frac{\Delta\alpha^2}{\sigma_\alpha^2} + \frac{\Delta\delta^2}{\sigma_\delta^2} \right)^{1/2}, \quad (2)$$

where $\Delta\alpha$ and $\Delta\delta$ are the position differences between the X-ray source and its optical counterpart in RA & DEC, and σ_α^2 and σ_δ^2 are the overall astrometric errors computed as $\sigma = (\sigma_X^2 + \sigma_{opt}^2)^{1/2}$. In this work, we assume $\sigma_X = 0.7$ arcsec and $\sigma_{opt} = 0.3$ arcsec. σ_X was calculated by square adding a systematic uncertainty of 0.5 and a centroiding error of 0.5 arcsec.

The likelihood ratio is defined as:

$$LR(r) = \frac{dp(r|id)}{dp(r|c)} = \frac{1}{2\lambda} e^{\frac{\lambda}{2}(2\lambda-1)} \quad (3)$$

where:

- $dp(r|id)$ is the *a priori* probability that an X-ray source and its optical counterpart have a separation between r , and $r + dr$ due to astrometrical errors
- $dp(r|c)$ is the probability that a confusing background optical object is found in the range r , and $r + dr$ from the X-ray source position.
- λ measures the number of confusing objects within the error circle and depends on the optical objects density (ρ_{opt}) as: $\lambda = \pi\sigma_\alpha\sigma_\delta\rho_{opt}$.

An optical source can be considered as a true counterpart of an X-ray source if its LR is higher than a certain threshold value L . L is obtained maximising the sum of completeness and reliability that are, in turn, mathematically defined in terms of the probabilities defined above. In our case, $L = 0.56$ and its corresponding variable is $r = 2.6$ which gives us a separation distance of 2.0 arcsec, a value consistent with the adopted one. The completeness of our detection is 98.3% (i.e. some 1 object lost due to the use of a particular cutoff value L), while reliability is 87.3% (~ 39 potentially false matchings).

3. Analysis

3.1. X-ray properties

We have computed the cumulative number count distributions ($\log N$ - $\log S$) per deg^2 in the soft band and compared it with other surveys in order to check the reliability of our source detections. We have chosen the soft band to be able to compare our distribution with that computed by Nandra et al. (2005) and those provided by other deep X-ray surveys, Chandra Deep Field South (CDFS, Giacconi et al. 2002), Chandra Deep Field North (CDFN, Alexander et al. 2003), ELAIS-N1 and ELAIS-N2 (Manners et al. 2003). All distributions are represented in Figure 4. For our sample two curves have been computed, one for the complete sample of X-ray detections and the other only for the X-ray detections that have optical counterparts. The median flux levels are 1.81×10^{-15} and $1.97 \times 10^{-15} \text{ erg cm}^{-2} \text{ s}^{-1}$, respectively. For the objects brighter than $\sim 10^{-14} \text{ erg s}^{-1} \text{ cm}^{-2}$ both distributions coincide, while for objects fainter than $\sim 10^{-14} \text{ erg s}^{-1} \text{ cm}^{-2}$ the density of X-ray sources with optical counterparts starts to decrease, since the optical sample is incomplete at the depth of our X-ray data. In general, at our flux limit the number counts of our complete X-ray sample are in good agreement with Nandra et al. (2005) and other surveys. We have detected a higher density of sources with flux below $\sim 5 \times 10^{-15} \text{ erg cm}^{-2} \text{ s}^{-1}$, most likely due to the use of different detection algorithms and more sensitive detection threshold. As we already mentioned, our threshold is 2×10^{-7} , two times higher than the one chosen by Nandra et al. (2005) (see 2.1.2 for more information).

Three independent energy bands, soft, hard2 and vhard (see the Section 2.1.1 for ranges), have been used to obtain the X-ray color-color diagram shown in Figure 5. Hardness ratios have been calculated as described in Section 2.1.2. X-ray sources are superimposed on a model grid computed using power law Spectral Energy Distributions (SEDs) with different photon indexes, Γ , affected by a galactic absorption column density, N_H , of $1.3 \times 10^{20} \text{ cm}^{-2}$ and different values of intrinsic absorption; the *Chandra* ACIS-I response matrices have been also included in the computa-

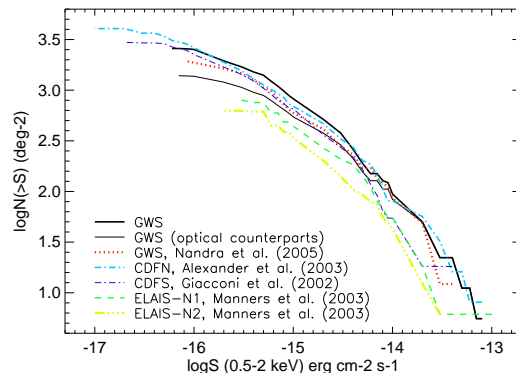


Fig. 4.— Cumulative $\log N$ - $\log S$ functions for the Groth field in the soft band, for all detected X-ray sources (thick solid line) and for X-ray sources with optical counterpart (thin solid line). Five distributions, with different exposure times and effective areas, have also been represented as comparison: GWS by Nandra et al. (2005) (dotted line), CDFN (thick dash-dot-dash line), CDFS (thin dash-dot-dash line), ELAIS-N1 (dash line) and ELAIS-N2 (dash-dot-dot-dash line)

tion. To obtain the fluxes we have used XSPEC (Arnaud 1996), varying the photon index between 0 and 3 with a step size of 0.5, and the intrinsic absorption column density between 20 and 24 (in logarithmic scale) in steps of 0.5. The majority of our sources are located within the model grid region, suggesting that their X-ray SED is compatible with the assumed model. A specially high concentration of objects can be seen in the region of N_H between 10^{20} and $5 \times 10^{21} \text{ cm}^{-2}$ and with $\Gamma \simeq 1.8$. A group of sources are located outside the model grid, showing a soft excess, suggesting that they can not be properly described by a single power law. For the fitting of these objects probably more components should be added.

3.2. Optical structural parameters

We obtained a set of structural parameters of the optical counterparts of our X-ray sample, in order to describe quantitatively their structure and morphology. In this section we describe the procedure used to derive the parameters and to produce a morphological classification.

We used SExtractor v2.2.2 (Bertin & Arnouts

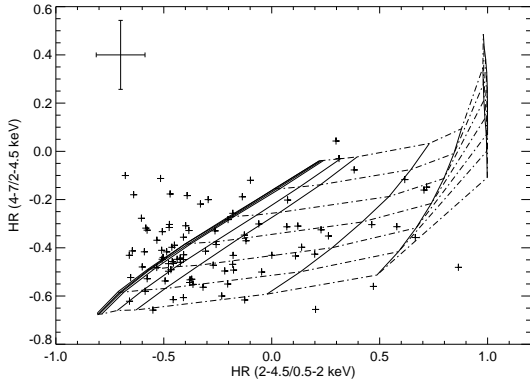


Fig. 5.— X-ray color-color diagram based on 2–4.5/0.5–2keV (HR'_1) vs. 4–7/2–4.5keV (HR'_2) hardness ratios. X-ray sources (crosses), from the complete X-ray catalog, are represented and superposed on an absorbed power law model grid. Photon index is varying between 0 and 3 in steps of 0.5 (dashed lines from up to down) and a $\log(N_H)$ between 20 and 24 in steps of 0.5 (solid lines from left to right). Median error bars are represented in the upper left corner of the diagram.

1996) to detect and extract the sources. Details of the source extraction process are provided in Cepa et al. (2008). The version used (v2.2.2) was modified by B. Holwerda to measure the Abraham concentration index (Abraham et al. 1994). This is defined as the ratio between the integrated flux within certain radius defined by the normalized radius α and the total flux. We used the values obtained at $\alpha = 0.3$ in our analysis in order to compare our results with those of Abraham et al. (1996). Another relevant output parameters for our study are the CLASS_STAR, which permits to roughly classify objects as compact or extended (for more information see Section 3.2.1), and the background that will be used later.

In addition, we used the Galaxy IMage 2D software package (GIM2D, Simard 1998; Simard et al. 2002) versions 2.2.1 and 3.1, to perform the galaxy structural parameter decomposition (see Figure 6). This software considers two components: an spheroid, represented by a Sérsic profile², and a disk represented by an

²While any rigorous analysis of the structural components of an AGN host should include an additional component,

exponential profile. Using the standard steps in DAOPHOT (Stetson 1987) we obtained the PSF images required for GIM2D execution. The initial parameters (including background estimation) and setup for GIM2D were determined using the images and catalogs produced by SExtractor (Bertin & Arnouts 1996). We obtained from the output provided by GIM2D the following parameters³: bulge-to-total ratio (B/T), residual parameter (R) (Schade et al. 1995, 1996), asymmetry (A) index (Abraham et al. 1994, 1996), the Sérsic index (n) and the total luminosity (L_{tot}). The residual parameter and the asymmetry index quantify the galaxy irregularity, by measuring the deviation from the simple, symmetric model (e.g. spheroid + disk), using as input the residual and original image, respectively. GIM2D also calculates for certain output parameters their lower and upper limits at 99% confidence level. In order to estimate the accuracy of the best fit parameters we have looked at the deviation, computed as the maximum between the best value and the upper or lower limits (see Figure 7). In this respect, the B/T parameter and Sérsic index have revealed inaccurate when applied to faint and small objects ($\lesssim 300$ pixel, while the seeing disk (FWHM) area is about 30 pixels) as shown in Figure 7. Therefore we have decided to do not use these parameters for the morphological classification.

In practice, we observed that the code either fails or produces unreliable output parameters in a number of cases: (1) when the source R magnitude is less than 18 or larger than 24, (2) when the isophotal area is very small (usually less than 90 pixels), (3) when the central object is surrounded by close neighbouring sources or nearby bright companions, and (4) when the source is close to

namely a pointlike nucleus, the small size of most of our objects compared with the seeing disk prevents from implementing such a detailed approach. Rather, we have simply assumed that the sum of the nuclear and bulge components can be roughly represented by a single Sérsic profile.

³According to the available documentation (Simard 1998; Simard et al. 2002), GIM2D calculates the Abraham concentration at four normalized radii $\alpha = 0.1, 0.2, 0.3$ and 0.4 . (Abraham et al. 1994, 1996). Comparing the results with the ones obtained with SExtractor, a systematic shift of ~ 0.2 is found towards larger values in GIM2D figures. After performing several tests we concluded that the GIM2D code performs its computations using normalized *area* rather than normalized *radius* against what is stated in the documentation.

the frame boundaries.

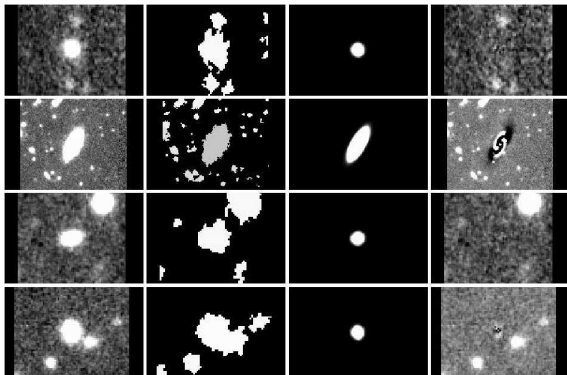


Fig. 6.— Four sample images of the GIM2D decomposition procedure. First column shows subimages (obtained from the scientific image) of objects to be fitted; the second column represents the mask subimages, third column shows the subimages obtained from the modelling and the fourth column shows the residual images, obtained from the original image after subtracting the model

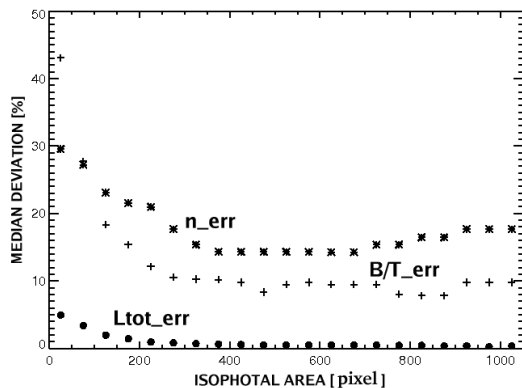


Fig. 7.— Evolution of the median error of the bulge-to-total ratio B/T (crosses), Sérsic index n (stars) and total flux (L_{tot}) as functions of the isophotal area. Deviations are evaluated as explained in Section 3.2.

3.2.1. Morphological classification

The selection of compact objects (QSOs, faint host AGNs or active stars) has been accomplished by using the SExtractor CLASS_STAR output parameter. The computed value depends on the

seeing, the peak intensity of the source and its isophotal area. The parameter ranges between 0 (extended object like a galaxy) and 1 (pointlike object). A source has been deemed as compact if its CLASS_STAR parameter is larger than 0.9.

To determine the morphology of extended objects (i.e. not selected as compact according to the criterion above), we analyzed four parameters: Abraham concentration index (C), Abraham asymmetry index (A), B/T ratio and residual parameter (R). We carried out the analysis in three different bands (B, V, and R) in order to determine the most reliable parameters, and the best band for morphological classification. We excluded I band here due to fringing.

We first classified each object using the set of parameters mentioned above, separately for each parameter in each band, considering the results from previous works as limits between different morphological types. We used the results of Im et al. (2002) and Simard (1998) to obtain preliminary morphology with the B/T parameter, Schade et al. (1995) results for the residual parameter and Abraham et al. (1996) for the classification with the concentration and asymmetry index. In practice, we found that, in many cases, different parameter sets lead to a different classification of a given object even in the same band. In order to have an independent evaluation criterion, we also carried out a visual classification of the objects. Despite its subjectiveness, this procedure can yield highest-quality results when applied to bright and extended objects, thus being a convenient method to test the reliability of the structural parameters that will be in turn applied to the analysis of fainter objects. The visual classification has been accomplished by inspection of the radial profile, 2D surface plot and isophotal contours diagram of each source (see Figure 8). For the dimmest and smallest objects of our sample (galaxies with the magnitude $R > 24$ and isophotal area < 100 pixels) the profiles and isophotal contours are too noisy to get an acceptable result by means of a simple visual inspection.

From this comparison we conclude that for our sample, characterised by faint objects (typically $R \gtrsim 22$) with small isophotal area ($\lesssim 300$ pixel, while the seeing FWHM disk area is about 30 pixels) the most reliable parameter is the concentration index C , combined either with the asymmetry index or

the residual parameter. We therefore based our morphological classification in the concentration index combined with both asymmetry index and residual parameter. The R band has been used, since, on the one hand, the largest part of optical counterparts have been found in this band, and on the other, the achieved S/N is generally larger. B, V, and I bands have been used to perform the morphological classification of objects not detected in the R band, or detected in this band but with very low S/N ratio.

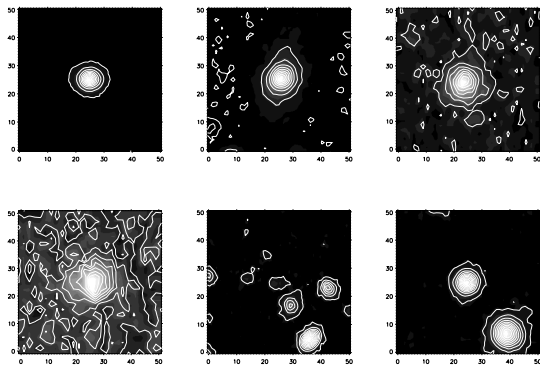


Fig. 8.— Sample of different Hubble type galaxies and their contour diagrams; Up: Left: Group I (E/S0), Center: group II (Early type spiral), Right: group III (Spiral); Down: Left, group III (Spiral), Center: group IV (Irr), Right: compact object ($C \geq 0.7$ or $CLASS_STAR > 0.9$). All objects are located in the center of the images.

Based on the classification using visual inspection of the brightest sample objects, and upon comparison with previous works (e.g. Abraham et al. 1996, see references above) in the present paper we created five categories or groups associating ranges of values of C with Hubble types:

- 0: $C \geq 0.7$ or $CLASS_STAR \geq 0.9 \rightarrow$ Compact obj.
- I: $0.45 \leq C < 0.7 \rightarrow$ E, E/S0 and S0
- II: $0.3 \leq C < 0.45 \rightarrow$ S0/S0a-Sa
- III: $0.15 \leq C < 0.3 \rightarrow$ Sab-Scd
- IV: $C < 0.15 \rightarrow$ Sdm-Irr

The first group is populated by elliptical and lenticular galaxies, whose profiles do not show any trace of disk or spiral arms (see Figure 8), the sec-

ond group includes very early spiral type galaxies which show signs of spiral arms. The third group comprises spiral galaxies while the fourth includes late type spirals and irregular galaxies, that show almost no regular form in their profiles. All galaxies, even those in the first group (elliptical and lenticular) have a concentration index $C \leq 0.7$, while all objects with $C > 0.7$ have been classified by SExtractor as compact ones, with the $CLASS_STAR$ parameter > 0.9 .

In Figure 9 we depict the Abraham asymmetry vs. concentration index diagram segregated according to the morphology determined using the visual classification for the brightest objects, and the structural parameters (in most of the cases C combined with A) for the fainter ones. Comparing our Figure 9 with that shown in Abraham et al. (1996), it can be seen that in our case there is a small shift of the concentration index towards smaller values. This can be explained considering the influence of the atmospheric seeing conditions. SExtractor does not apply any correction on the computed parameters for this effect, and as the seeing induced PSF increases, both concentration and asymmetry indexes tend to decrease, as confirmed by our simulations carried out by convolving simple galaxy models with seeing PSFs of different widths. Since the Abraham et al. (1996) diagram has been obtained from HST data, these differences are expected.

The morphological analysis described above has been applied to the complete sample of 340 X-ray objects with optical counterpart (see Figure 10). Of those, 333 were classified using the R band, 4 sources using the V band and finally 3 objects by means of B band data. The largest group (143 sources) is composed by compact objects (QSOs, faint host AGNs, stars) followed by group III (73 galaxies). 57 objects are found either in group II or III, having outstanding bulge component a signs of a formed disk and spiral arms. Only 33 galaxies are found to belong to the IV group. Finally, we detected 7 closed pairs, whose possible physical relation will be confirmed when photometric redshifts are computed (paper III, in preparation). Due to the high noise level, or to the presence of other objects close to the observed ones, the classification uncertainty for some of the objects is quite high, and it was not possible to determine

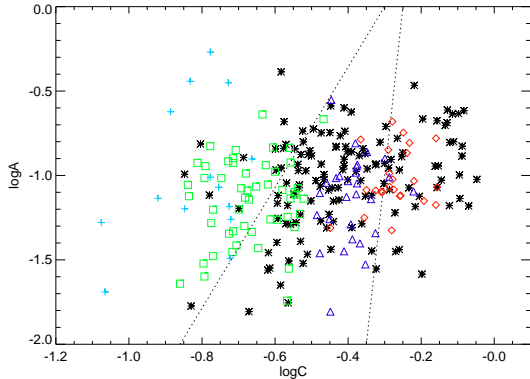


Fig. 9.— Morphological classification diagram combining the Abraham asymmetry index (A) vs. Abraham concentration index (C). Diamonds present E and S0 galaxies, triangles S0/S0a-Sa galaxies, squares young spiral galaxies (Sab-Sbcd) and crosses late type galaxies (Sdm-Irr). Compact objects are represented by star symbols. Dotted lines separate the loci of elliptical, spiral and peculiar galaxies (from right to left) obtained by Abraham et al. (1996). There is a small shift of our concentration and asymmetry index towards smaller values due to the influence of the atmospheric seeing conditions.

the morphological group: 3 galaxies could be either in group II or III and other 3 either in group III or IV. For 21 sources it was not possible to determine the morphology since they are at the detection limit.

4. Relationship between X-ray and optical structural properties

4.1. Nuclear classification

The simplest way to classify the nuclear type is based on the X-ray-to-optical ratio (X/O). The typical value of X/O flux ratios for X-ray selected AGN (both type 1 or BLAGN and type 2 or NLAGN) is in the range between 0.1 and 10 (e.g. Fiore et al. 2003). For optically selected type 1 AGNs the typical value is $X/O \simeq 1$ (Alexander et al. 2001; Fiore et al. 2003). At high X/O flux ratios (well above 10) we can find BLAGN and NLAGN as well as high-z high-luminosity obscured AGN (type 2 QSOs), high-z clusters of galaxies and extreme BL Lac objects.

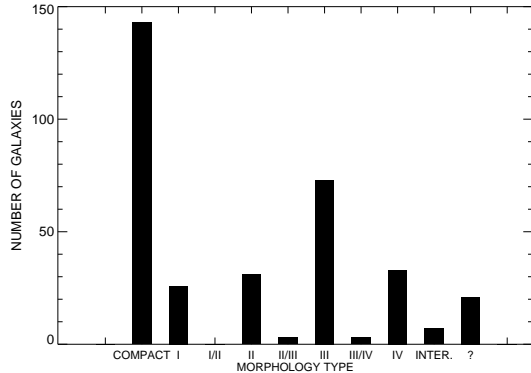


Fig. 10.— The histogram represents the final morphological classification of the GWS X-ray emitters with optical counterparts. Different values of the Abraham concentration index correspond to different groups I-IV (see text). A group of possible interacting objects has been detected; a group of sources (marked with '?') remained unidentified due to their very low S/N ratio.

Finally, the $X/O < 0.1$ region is typically populated by coronal emitting stars, normal galaxies (both early type and star-forming) and nearby heavily absorbed (Compton thick) AGN.

We have applied a simple criterion for performing a coarse nuclear-type classification of our sample objects, based on diagnostic diagrams relating X-ray-to-optical ratios (X/O) to hardness ratios (HR). This criterion is based on the results of Della Ceca et al. (2004) on the *XMM-Newton* Bright Serendipitous Survey; they found that, when plotting the $HR(2-4.5keV/0.5-2keV)$ (equivalent to our HR'_1) against X/O, computed as the ratio of the observed X-ray flux in the 0.5-4.5keV (soft+hard2) energy range and the optical R-band flux, most (85%) of the BLAGN identified by means of optical spectroscopy are tightly packed in a small rectangular region of the diagram, while NLAGN (type 2) tend to populate a wide area of the diagram (towards harder values of the hardness ratio). We applied the same approach to our sample, combining the HR'_1 hardness ratio with the X/O ratio, where the optical flux F_R has been derived from the Petrosian magnitudes in the R band. The resulting diagram, that also includes host morphology information, is shown in Figure 11, where the dashed-

line box indicates the locus of the BLAGN region. We set the right edge of this box, $\text{HR}(2 - 4.5\text{keV}/0.5 - 2\text{keV}) \approx -0.35$ as a coarse boundary separating 'unobscured' AGN (BLAGN) and 'obscured' AGN (NLAGN). On the other hand, we consider the small box depicted in the diagram as the "highest probability" region for finding a BLAGN (Della Ceca et al. 2004). We find that a large fraction of our objects, 63%⁴, fall inside the region of BLAGNs, while 51% of the sample is placed within the small BLAGN box defined by Della Ceca et al. (2004). Regarding morphology, we do not find evidence of any relationship between nuclear and morphological types, since we did not obtain any clear separation of nuclear species based on morphological type. Nevertheless, we can see that the majority of objects identified as compact (65%) are placed in the BLAGN region. It is also interesting to highlight the relationship between the X/O ratio and the host galaxy morphology, with early-type galaxies having generally lower values for X/O ratio and an opposite behavior of late-type objects. Finally, we find that only about 7% of our sample objects are placed in the lower region of the diagram (i.e. that typical of stars/normal galaxies/Compton-thick AGN).

We also represented the X/O ratio with respect to HR_1 , yielding a basically identical distribution as that described above, and with respect to HR_2 and HR'_2 , observing that in these two cases is harder to get a clear separation between different nuclear/morphological types; this behavior is expected since hardness ratios computed from the hard and vhard bands are less sensitive to absorption than those involving the soft band, which is one of the main criteria for the separation between broad and narrow line AGN.

4.2. X-ray and optical properties

We combined the X/O ratio with optical colors (B-R and B-I) for the different morphological groups and nuclear types, as shown in Figure 12. We observe that compact and late-type objects tend to show bluer colors, while early-

⁴All fractions given here are relative to the total number of X-ray objects having optical counterpart and detected in both soft and hard2 energy bands such as $\text{HR}(2 - 4.5\text{keV}/0.5 - 2\text{keV})$ can be computed

type galaxies tend to present redder colors and also lower X/O values, as expected. On the other hand, there is a mild tendency for BLAGN to show bluer colors than those found in NLAGN, as already observed in local universe samples (e.g. Yee 1983; Sánchez-Portal et al. 2004). The B-R average value for BLAGNs is 1.0 and for NLAGNs 1.4, with $\sigma = 0.5$ and 0.6 respectively. Using the Kolmogorov-Smirnov test, the two distributions are statistically different with a significance level of 99%.

When representing the X/O ratio vs. the Abraham concentration index C we find a strong anticorrelation between these two parameters (Figure 13), obtaining a correlation coefficient of ~ -0.5 . Using Spearman and Kendall (S-K) statistics, we obtained a correlation significance level $>99\%$. The first order polynomial function has been fitted with a slope of -2.03, log X/O-intercept of -0.94 and a standard deviation of ~ 0.5 . This result is consistent with that referred above and depicted in Figure 11, that is the tendency of early-type galaxies to have lower than average X/O values and the opposite behavior in late-type ones. As seen in Figure 13, all morphological groups, including compact objects, tend to follow the same relation. For compact objects we obtained similar parameters using S-K statistics: a correlation coefficient of ~ 0.5 and a correlation significance level $>99\%$. A least squares fit gives to the anticorrelation a slope of -2.4 and a log X/O-intercept of -0.95. Comparing different nuclear types, we found that both BLAGN and NLAGN follow the same distribution (see Figure 13). On the other hand, we did not find any clear correlation between $\text{HR}(2 - 4.5\text{keV}/0.5 - 2\text{keV})$ and the concentration index (Figure 14), suggesting that the observed anticorrelation is not related to obscuration.

The physical origin of the observed anticorrelation is not well established. First of all, it is not easy to disentangle possible bias effects that superimposed to variable seeing conditions. It has been pointed out the existence of redshift-dependent biases in both A and C, due to the reduction of apparent size and surface brightness with respect to the sky background with increasing z, along with poorer sampling and lower S/N (Brinchmann et al. 1998; Conselice et al. 2003);

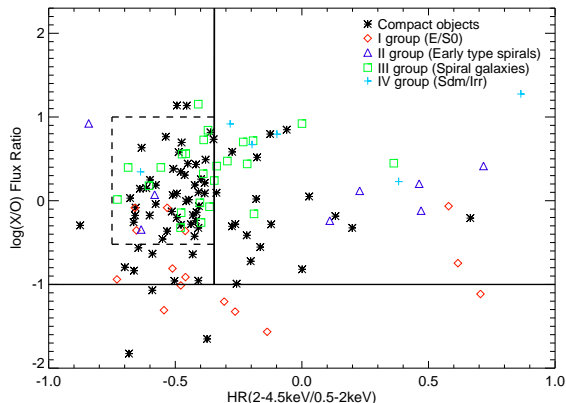


Fig. 11.— Relationship between X/O ratio and $HR(2 - 4.5keV/0.5 - 2keV)$, for the different morphological types. Solid lines separate BLAGN and NLAGN regions and the area with $X/O < 0.1$, where stars, normal galaxies and Compton thick AGNs can be found (Fiore et al. 2003). Dashed line box presents the limits obtained by Della Ceca et al. (2004) where $\sim 85\%$ of their spectroscopically identified BLAGN have been found. In our case, inside of this box can be found $\sim 51\%$ of all objects from the diagram.

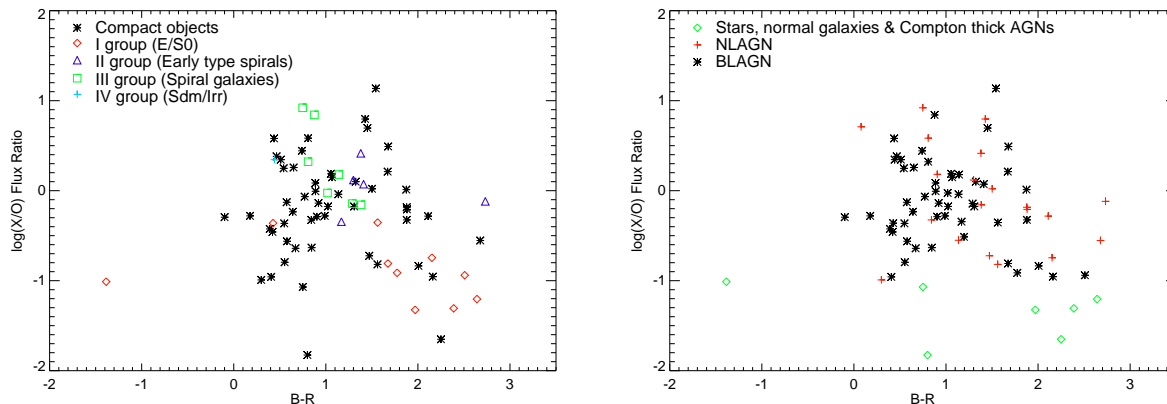


Fig. 12.— $\log(X/O)$ flux ratio vs. B-R color for different morphology (left) and nuclear types (right).

on the other hand, there is a “bandpass shift” with respect to the rest wavelength (Bershady et al. 2000). Even if these effects combine to produce some uncertainty in the morphological classification of galaxies, generally in the sense of shifting objects to apparently later Hubble types (i.e. with lower C values), A and C seems to be reproducible out to $z=3$, within a reasonable scatter (Conselice et al. 2003). Moreover, there can be a truly evolutionary effect in the AGN host galaxies, indicating that galaxies at higher redshift are intrinsically less concentrated (Grogin et al. 2005).

At this stage we cannot apply any correction

which depends on the redshift, although this is one of the objectives for the future work. However, we have performed a preliminary evaluation by representing the concentration index C versus the spectroscopic redshifts z gathered from the DEEP2 catalog for 84 objects from our sample. While for non compact objects we obtained an anticorrelation between these two parameters, C and z are found uncorrelated for compact objects, in clear contrast with the observed behavior in Figure 13.

So, although the biases described above might contribute partially to it, the observed anticorre-

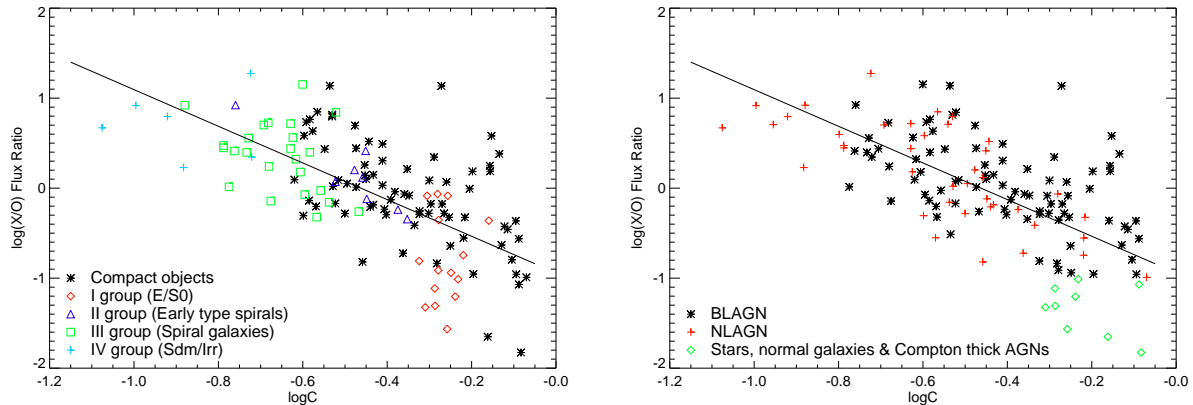


Fig. 13.— Relationship between X/O and the Abraham concentration index C for different morphological (left) and nuclear types (right). A clear anticorrelation is observed.

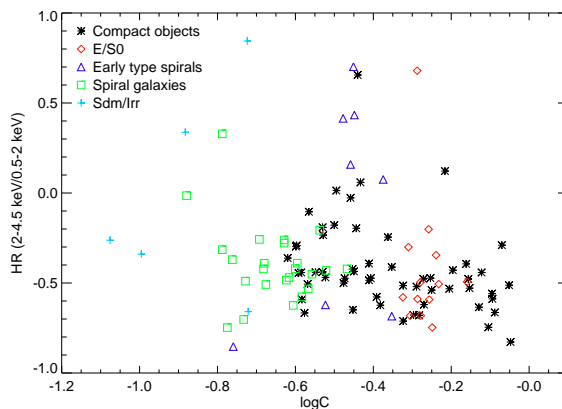


Fig. 14.— Relationship between the hardness ratio $HR(2-4.5\text{keV}/0.5-2\text{keV})$, and the concentration index C for the different morphological types.

lation seems to also be a result of a true physical effect. In order to attempt to explain it, we have first to understand the physical connections of the two observables C and X/O. The concentration index (C) is tightly linearly correlated to the central velocity dispersion (Graham et al. 2001a,b), which is in turn related to the nuclear black hole (BH) mass (e.g. Magorrian et al. 1998). Therefore, the concentration and the nuclear BH mass (M_{BH}) are correlated. The physical connections of the X-ray to optical flux ratio are not so evident. The X/O ratio measures the X-ray flux (in the 0.5-4.5keV band), normalized with the R-band optical flux of the whole galaxy (nucleus, bulge and disk). It should be noted that no band-

pass, or K-correction is performed; therefore if the sample spans a large redshift range the interpretation of the quantity becomes more problematic. If the nuclear luminosity is large compared with that of the host galaxy, X/O ratio can be thought as a measure of the X-ray to optical spectral index, α_{OX} ⁵. This parameter has been found to be strongly anticorrelated with the UV luminosity $L_{2500\text{\AA}}$, without a significant correlation with redshift (Steffen et al. 2006). On the other hand Bian (2005) found a strong correlation between the hard/soft X-ray spectral index, α_X and the

⁵This relation is usually defined as $\alpha_{OX} = 0.3838 \log(f_{2\text{keV}}/f_{2500\text{\AA}})$

Eddington ratio in a sample of 41 BLAGN and narrow-line Seyfert 1 (NLS1) galaxies observed with ASCA. Other works have confirmed this correlation (Grupe 2004; Shemmer et al. 2006). The relationship between α_X and α_{OX} has not been thoroughly studied in large samples of AGN, but a linear correlation has been found between both spectral indexes in a sample comprising 22 out of 23 quasars in the complete the Palomar-Green X-ray sample with $z < 0.4$ and $M_B < -23$ (Shang et al. 2007). If this last correlation holds for our sample, X/O could be tracing the Eddington ratio in the large nuclear luminosity limit. In addition, if the host galaxy luminosity is large when compared with the nuclear luminosity ($L_{bulge+disk} \gg L_{nucleus}$), the X/O ratio can be thought as a lower bound of the X-ray-to-bulge luminosity ratio, that is in turn a (weak) measure of the AGN Eddington ratio $L/L_{Edd} \propto L/M_{BH}$, assuming that the X-ray luminosity represents the nuclear luminosity and the bulge luminosity is proportional to the bulge mass (and therefore to M_{BH}).

Hence, we can guess a (loose) correlation between X/O and the energy production efficiency of the AGN. Under these assumptions, the C vs. X/O relation traces the correlation between the Eddington ratio and the nuclear BH mass. The obtained result could therefore suggest that early-type galaxies, having poor matter supply to feed the activity, have lower Eddington rates than those of late-type, with larger reserves of the gas for AGN feeding.

This suggested approach is consistent with the results obtained by Ballo et al. (2006, 2007) in a sample of X-ray selected AGNs at $z \leq 1$. They observed that a large fraction of low-luminosity AGNs are fed by black holes with a mass $M_{BH} > 3 \times 10^6 M_\odot$, and Eddington rate $\ll 1$, while a small ($< 10\%$) fraction of AGNs host small SMBH ($M_{BH} < 10^6 M_\odot$) and Eddington rate ≈ 1 , which corresponds to a more efficient accretion rate. They stated that their results strongly suggest that most of the low-luminosity X-ray selected AGNs (at least up to $z \leq 0.8$) are powered by rather massive black holes, experiencing a low-level accretion in a gas-poor environment.

Our approach is also consistent with the results of Wu & Liu (2004), who studied the black

hole masses and Eddington rates of a sample of 135 double-peaked broad line AGNs, observed in two surveys: SDSS and a survey of BLAGN radio emitters. They obtained that if the separation between the line peaks (which is correlated to the SMBH mass) decrease, the Eddington rate increases.

Kawakatu et al. (2007) found an anticorrelation between the mass of a SMBH and the luminosity ratio of infrared to active galactic nuclei Eddington luminosity, L_{IR}/L_{Edd} , for a sample of ultraluminous infrared galaxies with type 1 Seyfert nuclei (type 1 ULIRGs) and nearby QSOs, which also could be consistent with our approach. The anticorrelation is interpreted as a link between the mass of a SMBH and the rate of mass accretion onto a SMBH, normalized by the AGN Eddington rate, which indicates that the growth of the black hole is determined by the external mass supply process, and not the AGN Eddington-limited mechanism, changing its mass accretion rate from super-Eddington to sub-Eddington.

5. The clustering of X-Ray emitters and extended optical counterparts

The study of large-scale environmental conditions of AGN host galaxies are useful not only for understanding the differential properties of the AGN phenomena, but to trace the formation and evolution of such galaxies and the structures where they reside. Despite the relevance of X-ray selected AGNs, their clustering properties still remain quite unknown (Basilakos et al. 2005, and references therein). In this sense, and taking into account the characteristics of the X-ray source catalog presented in this work, we have calculated the 2-point angular correlation function (2p-ACF) for significant subsamples.

The 2p-ACF, $\omega(\theta)$, gives the excess of probability, with respect to a random homogeneous distribution, of finding two sources in the solid angles $d\Omega_1$ and $d\Omega_2$ separated by an angle θ , and it is defined as

$$dP = \mathcal{N}^2 [1 + \omega(\theta)] d\Omega_1 d\Omega_2 \quad (4)$$

where \mathcal{N} is the mean number density of cataloged sources. To measure the 2p-ACF we have followed the same procedure as done in Cepa et al. (2008), adopting the estimator of Landy & Szalay (1993),

which can be written in the form

$$\omega(\theta_i) = \frac{DD - 2DR + RR}{RR} \quad (5)$$

where $DD = N_{ss}(\theta_i)$ is the fraction of possible *source-source* pairs counted in i -bins over the angular range studied and $DR = \left[\frac{(N_g - 1)}{2N_r} \right] N_{gr}(\theta_i)$, $RR = \left[\frac{N_s(N_s - 1)}{N_r(N_r - 1)} \right] N_{rr}(\theta_i)$ are the normalized counts of *source-random* and *random-random* pairs in these bins, respectively. To make the random catalogs we placed $(200 \times N_{source})$ random points by following the X-ray source angular distribution. However, the source density is affected by several instrumental biases such as detector gaps and sensitivity variations due to survey regions with different exposure times. To account for these effects, we made normalized sensitivity maps from the effective exposure time and source distributions for each band used in this section (soft and hard2). The raw maps were modelled using a minimum-curvature algorithm. Next, the uniform density random catalogs were convolved with the corresponding sensitivity map to obtain differential number counts in the surveyed area. In the case of the HR(2–4.5keV/0.5–2keV) catalog, we adopt the sensitivity map used for the hard2 source one. The smoothed footprint of each sensitivity map can be seen in Figure 15.

We measure $\omega(\theta_i)$ in i -logarithmic bins of width $\Delta(\log \theta) = 0.2$ in the angular scales $0.24 \leq \theta \leq 24.0$ arcmin. The lower limit in angular separation is according to the minimum detection scale defined in the Section 2.1.2. The formal error associated with the 2p-ACF measured is the Poissonian estimate $\sigma_\omega^2 = \frac{1 + \omega(\theta_i)}{DD}$. The 2p-ACF binned measures were fitted using the $A_\omega(\theta^{1-\gamma} - C)$ power law. We adopted a fixed canonical slope $\gamma=1.8$ (the so called “comoving clustering model”) and C is defined as

$$C = \frac{\sum N_{rr}(\theta) \theta^{-0.8}}{\sum N_{rr}(\theta)} \quad (6)$$

corresponding to the numerical estimation of the “integral constraint” (Peebles 1980). As in Miyaji et al. (2007), we use the normalization A as the fitting parameter rather than the correlation length $\theta_c = A^{1/(\gamma-1)}$, since the former gives better convergence of the fit.

From the whole catalog we have selected the soft (0.5–2 keV) and hard2 (2–4.5 keV) sources

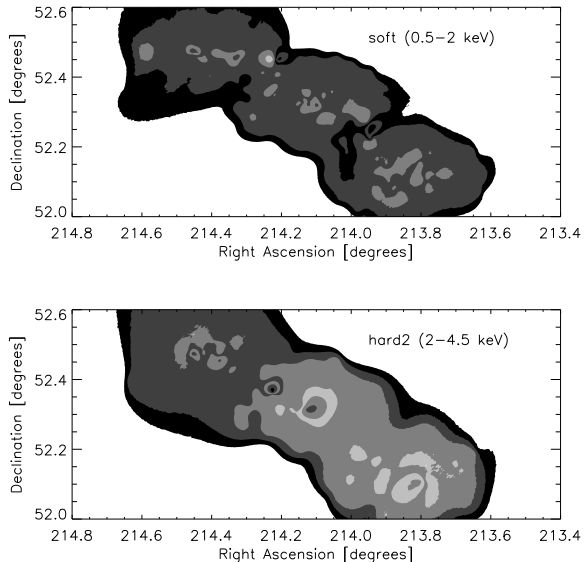


Fig. 15.— Smoothed sensitivity maps in the soft (0.5–2 keV) and hard2 (2–4.5 keV) bands, used to convolve the uniform density random catalogs. The sensitivity dimension is normalized to the maximum exposure time in each band. Contours are linearly binned and lighter regions correspond to higher sensitivities.

(given their similar depths in the survey), the X-ray objects with $HR(2 - 4.5keV/0.5 - 2keV) \neq 0$ and the fraction of X-ray sources with optical counterparts. Table 2 summarizes the basic results of the correlation analysis for these subsamples. In all cases, we have obtained significant positive clustering signal. Regarding the soft band sample, the correlation length θ_c derived from A_ω is consistent with the obtained by Basilakos et al. (2005) (XMM-Newton LSS) and it is $\sim 2\sigma$ larger than the values obtained by Gandhi et al. (2006), Carrera et al. (2007) and Ueda et al. (2008). In the specific case of the hard2 band, we only found in the literature the 2p-ACF estimations of Miyaji et al. (2007), valid for X-ray sources detected in the XMM-Newton observations of the COSMOS field and corresponding to their MED band: our fitted correlation length is ~ 4.3 times larger, although our sample is a factor 2 deeper.

In Figure 16 are represented our 2p-ACF measurements with the best-fit $A_\omega \theta^{-0.8}$ power-law

Table 2: Clustering properties of the X-ray selected sources. N_{source} is the number of data points used in the 2p-ACF estimation and A_ω is the best-fit value in the separation range given by $\theta_{\min} - \theta_{\max}$, assuming a power-law $\omega(\theta) = A_\omega \theta^{(1-\gamma)=-0.8}$. The goodness-of-fit statistics (χ^2) and the fitted 2p-ACF at 1 arcmin [$\omega(1')$] are given in the final columns. The errors represent 1σ uncertainties.

Subsample	N_{source}	$\theta_{\min} - \theta_{\max}$ arcmin	A_ω ($1 - \gamma = -0.8$) $\times 10^{-3}$ degrees	χ^2	$\omega(1')$
soft (0.5-2 keV)	465	0.24-24.0	6.99 ± 0.68	0.030	0.15 ± 0.02
hard2 (2-4.5 keV)	266	0.24-24.0	9.19 ± 1.28	0.107	0.20 ± 0.03
HR _(2-4.5keV/0.5-2keV)	190	0.24-24.0	9.68 ± 1.30	0.109	0.21 ± 0.03
Optical counterparts ($I \leq 23$)	104	0.60-24.0	19.99 ± 3.32	0.096	0.42 ± 0.07

in soft and hard2 bands (panels a and b, respectively). It is noticeable that the clustering amplitude obtained in both bands looks similar. Thus, in the case of the Groth field, we would not expect redshift or spatial clustering differential effects in the soft and hard2 band samples. Interestingly, an absence of correlation in differently defined hard bands has been reported by Gandhi et al. (2006) and Puccetti et al. (2006); nevertheless, Yang et al. (2003) and Basilakos et al. (2004) not only yield a positive correlation amplitude, but the hard band signal is several times that of the soft band. Other results with similar correlation lengths in both bands are given by Carrera et al. (2007), Miyaji et al. (2007) and Yang et al. (2006).

In the panel c of Figure 16 is represented the 2p-ACF estimations for a HR(2-4.5keV/0.5-2keV) selected sample. The clustering amplitude is slightly larger than the soft or hard2 band ones. Moreover, the whole HR(2-4.5keV/0.5-2keV) subsample was decomposed using the boundary referred in Sect. 4.1 to separate type 1 (or BLAGN) from type 2 (or NLAGN) populations and a positive, very similar clustering signal from both subsamples emerged from the 2p-ACF estimations, despite their goodness-of-fit statistics are worse than the tabulated values in a factor ~ 1 because of the small size of the subsamples.

Finally, we measured the 2p-ACF of the optical counterparts of X-ray sources in order to compare the clustering behavior with those that come from the analysis of galaxy populations in the same field. For a reliable comparison is necessary to discard the compact objects (i.e. with

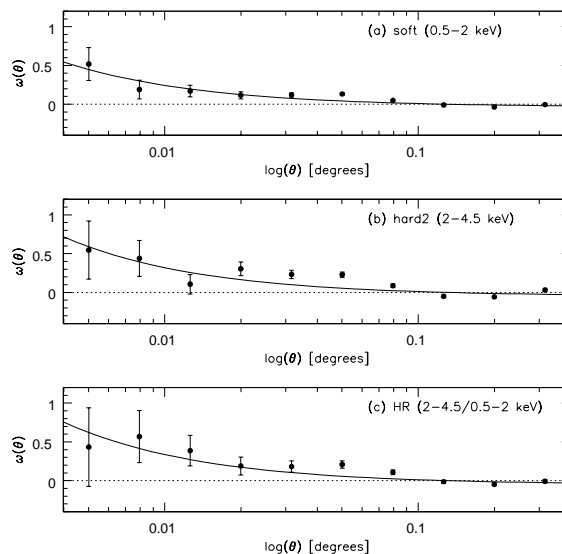


Fig. 16.— 2p-ACF estimates of the X-ray sources detected in the soft band (panel a), hard2 band (panel b) and HR as defined in eq. 1 (panel c). The continuous line represents the $A_\omega \theta^{(1-\gamma)=-0.8}$ power law fit to the data.

CLASS_STAR>0.9) from the optical counterparts catalog, as well as all objects fainter than a limiting magnitude. We have selected the peak of the apparent brightness distribution in the I-band as such limiting magnitude. Thus, X-ray counterparts with $I > 23$ were ruled out, remaining 104 extended objects, which can be regarded as AGN host candidates of the corresponding X-ray sources.

In spite of this skinny sample, it is possible to obtain some interesting lines of thought about the X-ray selected AGN clustering. It is suggested that the typical environments of AGNs are no different to those of inactive galaxies in general, at redshift ranges above $z \sim 0.4$ (e.g. Grogin et al. 2003; Waskett et al. 2005). Nevertheless, Coil et al. (2004) and Gilli et al. (2005) have argued that the AGN are preferentially hosted by early-type galaxies at a typical redshift of ~ 1 . In this way, Basilakos et al. (2004) found that clustering length values of hard X-ray objects are comparable with those of Extremely Red Objects (EROs) and luminous radio sources. More recently, Georgakakis et al. (2007) demonstrated that X-ray-selected AGNs at $z \sim 1$, in the AEGIS field, avoids underdense regions at 99.89% of significance.

In Figure 17 we have depicted the 2p-ACF of the optical counterparts selected as described above. The 2p-ACFs of the Groth field galaxy sample with $I \leq 23$ only and with $V-I > 3$ ($I \leq 24$) from Cepa et al. (2008) are overplotted. At least in the range $0.01 \leq \theta \leq 0.1$ degrees, the clustering signal produced by the optical counterparts of our X-ray sources is 1-2 σ stronger than the corresponding to the $I \leq 23$ galaxy population. In terms of fitted correlation length, the $\theta_c(\text{X-ray})$ ($1-\gamma = -0.8$) is ~ 30 times larger than that of the Groth field galaxies, but only ~ 2.3 times larger than the maximum correlation length of the $V-I > 3$ galaxies in the same field. In the other hand, using the optical data from the counterparts catalog, we found that the median $V-I$ observed color is 1.86 and most of 65% of the optical counterparts have an observed color $V-I > 2$. This means that a significant population of our optical counterparts is a composition of red and very red galaxies, whereas its clustering signal tends to reproduce that associated with such galaxies, which drive the $\sim 10x$ clustering excess found by Cepa et al. (2008). At once, more than a 55% of the optical counterparts belong to the morphological categories I and II, as defined in the Section 3.2.1.

6. Summary and Conclusions

We processed and analyzed public, 200 ksec *Chandra*/ACIS observations of three fields comprising the original GWS gathered from the *Chan-*

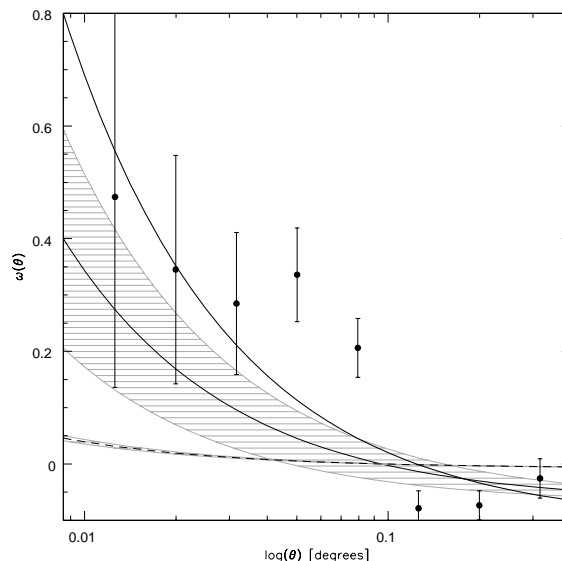


Fig. 17.— 2p-ACF estimation for the optical extended ($\text{CLASS_STAR} \leq 0.9$) counterparts with I magnitude brighter than 23 (solid circles). The continuous thick line represents the $A_\omega \theta^{(1-\gamma)=-0.8}$ power law fit to the data. The dashed line represents the 2p-ACF estimation for galaxies with $I \leq 23$ in the Groth field, whereas the continuous thin line it does for the $V-I > 3$ color selected galaxies with $I \leq 24$, both extracted from Cepa et al. (2008). The shaded regions represent fitting errors of 1σ .

dra Data Archive, combined with our broadband survey carried out with the 4.2m WHT at La Palma. Our X-ray catalog contains 639 unique X-ray emitters, with a limit flux at 3σ level of $4.8 \times 10^{-16} \text{ erg cm}^{-2} \text{ s}^{-1}$ and a median flux of $1.81 \times 10^{-15} \text{ erg cm}^{-2} \text{ s}^{-1}$ in the full (0.5-7 keV) band. Cross-matching the X-ray catalog with our optical broadband catalog, we have found 340 X-ray emitters with optical counterparts. The completeness and the reliability of cross-matching procedure are 97% and 88.9%, respectively. At our flux limit, the number counts of our complete X-ray sample are in good agreement with Nandra et al. (2005) and other comparison surveys mentioned in Section 3.1. X-ray SEDs of the majority of our sources are compatible with the power law model, affected with the galactic absorption column density and the intrinsic absorption. We

have performed a morphological classification obtaining and analyzing different structural parameters, including the bulge-to-total ratio, residual parameter, Sérsic index, asymmetry and concentration indexes. We also performed the classification based on visual inspection. To obtain the nuclear classification, we applied a criterium based on the correlation between X/O flux ratio and HR1' hardness ratio. 63% of our sources, with $HR1' \neq 0$, have been classified as BLAGNs. The electronic table summarizes the X/O flux ratios, HR1' values and morphological classification of all 340 X-ray emitters with optical counterparts. We have investigated the correlations between X-ray and broadband optical structural parameters that provide with information about the host galaxy morphology and populations, finding that:

1. For a sample where most of the objects are faint ($R \geq 22$) and with small isophotal area (≤ 300 pixels), bulge-to-total flux ratio has revealed inaccurate to perform the morphological classification. Concentration index combined with the asymmetry index have been found to provide the best separation criterion for such a sample. different morphological types have been observed to distribute according to the following ranges of concentration index: group 0 (compact objects) $\rightarrow C \geq 0.7$ (or $CLASS_STAR \geq 0.9$), group I (E, E/S0 and S0) $\rightarrow 0.45 \leq C < 0.7$, group II (S0/S0a-Sa) $\rightarrow 0.3 \leq C \leq 0.45$ (0.47), group III (Sab-Scd) $\rightarrow 0.15 \leq C \leq 0.3$ and group IV (Sdm-Irr) $\rightarrow C \leq 0.15$

2. No clear separation has been found between the morphology and the nuclear type, but most of our objects classified as compact are placed in the region of BLAGNs.

3. We can confirm the tendency of compact and late type objects to show bluer colors, while early type galaxies tend to present redder colors. On the other hand, we find a mild tendency of BLAGNs to show bluer colors when compared with NLAGNs.

4. We obtained an anticorrelation between the X-to-optical flux ratio and the concentration index (which parametrizes the morphology), with significance level higher than 99%, showing that the early-type galaxies tend to have lower and the late-type galaxies higher than average X/O values. Objects classified as compact show this anticorrelation as well, with the same significance level. The anticorrelation might suggest that early-type galaxies, having poor matter supply to feed the ac-

tivity, have lower accretion rates than those of late type, with larger reserves of gas for AGN feeding.

Finally, we presented the first results on the two-point angular correlation function of the X-ray selected sources in the Groth field from *Chandra*/ACIS observations, segregated in four subsamples: soft, hard2, $HR_{(2-4.5keV/0.5-2keV)}$ and optical extended counterparts. We obtain the following results and conclusions:

1. All subsamples reveal a significant positive clustering signal in the ~ 0.5 to 6 arcmin separation regime. Canonical power-law ($\gamma=1.8$) fits to the angular correlation functions have been made, obtaining correlation lengths between ~ 7 and 27 arcsec, depending on the subsample.

2. We have neither found substantial differences between the clustering of soft and hard2 selected X-ray sources, nor when comparing the populations of type 1 and type 2 AGN (i.e. 'unobscured' and 'obscured' AGN, respectively), separated using the $HR_{(2-4.5keV/0.5-2keV)} \approx -0.35$ boundary.

3. The clustering analysis of the optical counterparts of our X-ray emitters provides a correlation length significantly larger than the one found for the whole galaxy population with the same limiting magnitude, and same field, but similar to that of strongly clustered populations like red and very red (bulge-dominated) galaxies. A clustering signal $> 1\sigma$ was observed even at $\theta \sim 30$ arcsec, which corresponds to $160 h^{-1}$ kpc, assuming a mean redshift of 0.85 for *Chandra* extragalactic sources (Hasan 2007). This comoving distance is, for instance, comparable to the separation of two mergers in the $t \approx 2$ Gyr stage of their large-scale evolution, according to the model of Mayer et al. (2007) on rapid formation of SMBH. Hence, our results suggest that the environment plays an important (but not unique) role as possible triggering mechanism of AGN phenomena. This fact can be perfectly compatible with the interpretation given to the anticorrelation between X/O ratio and the concentration index. The former may be associated to the genesis of the AGNs, while the anticorrelation could be that to their maintenance and evolution.

7. Acknowledgements

This work was supported by the Spanish *Plan Nacional de Astronomía y Astrofísica* under grants AYA2005-04149 and AYA2006-2358. JIGS and JGM acknowledge financial support from the Spanish Ministerio de Educación y Ciencia under grants AYA2005-00055 and AYA2006-2358, respectively.

This research has made use of software provided by the Chandra X-ray Center (CXC) in the application packages CIAO and ChIPS.

IRAF is distributed by the National Optical Astronomy Observatory, which is operated by the Association of Universities for Research in Astronomy (AURA) under cooperative agreement with the National Science Foundation.

This publication makes use of data products from the Two Micron All Sky Survey, which is a joint project of the University of Massachusetts and the Infrared Processing and Analysis Center California Institute of Technology, funded by the National Aeronautics and Space Administration and the National Science Foundation.

We would like to thank Laura Tomás who kindly provided us with her software for diagnosis of hardness ratios using model grids.

We acknowledge support from the Faculty of the European Space Astronomy Centre (ESAC).

REFERENCES

- Abraham, R. G., van der Bergh, S., Glazebrook, K., Ellis, R. S., Santiago, B. X. & Surma, P. 1996, *ApJ*, 107, 1
- Abraham, R. G., Valdes, F., Yee, H. K. C., & van der Bergh, S. 1994, *ApJ*, 432, 90
- Alexander, D. M., Brandt, W. N., Hornschemeier, A. E., Garmire, G. P., Schneider, D. P., Bauer, F. E., & Griffiths, R. E. 2001, *AJ*, 122, 2156
- Alexander, D. M., Bauer, F. E., Brandt, W. N., Schneider, D. P., Hornschemeier, A. E., Vignali, C., Barger, A. J., Broos, P. S., Cowie, L. L., Garmire, G. P., and 4 coauthors 2003, *AJ*, 126, 539
- Arnaud, K. A. 1996, *ASPC*, 101, 17
- Ballo, L., Cristiani, S., Fasano, G., Fontanot, F., Monaco, P., Nonino, M., Pignatelli, E., Tozzi, P., Vanzella, E., Fontana, A., Giallongo, E., Grazian, A., & Danese, L. 2007, *ApJ*, 667, 97
- Ballo, L., et al. 2006, Proceedings of the The X-ray Universe 2006 (ESA SP-604), ESA-SP.604..595B
- Barcons, X. et al. 2007, *A&A*, 476, 1191
- Barger, A. J., et al. 2003, *AJ*, 126, 632
- Basilakos, S., Georgakakis, A., Plionis, M., & Georgantopoulos, I. 2004, *ApJ*, 607, L79
- Basilakos, S., Plionis, M., Georgakakis, A., & Georgantopoulos, I. 2005, *MNRAS*, 356, 183
- Bershady, M. A., Jangren, A. & Conselice, C. J., 2000, *AJ*, 119, 2645
- Bertin, E. & Arnouts, S. 1996, *A&AS*, 117, 393
- Bian, W. H., 2005, *A&AS*, 5, 289
- Brandt, W. N., & Hasinger, G. 2005, *ARA&A*, 43, 827
- Brinchmann, J., Abraham, R., Schade, D., Tresse, L., Ellis, R. S., Lilly, S., Le Fèvre, O., Glazebrook, K., Hammer, F., Colless, M., Crampton, D., Broadhurst, T., 1998, *ApJ*, 499, 112
- Cappelluti, N., et al. 2007, *ApJS*, 172, 341
- Capak, P. et al. 2007, *ApJS*, 172, 99
- Carrera, F. J., et al. 2007, *A&A*, 469, 27
- Cepa, J., Pérez García, A. M., Bongiovanni, A., Alfaro, E., Castañeda, H. O., Gallego, J., González-Serrano, J. I., Sánchez-Portal, M., González, J. J. 2008, *A&A*, 490, 1
- Cepa, J., Alfaro, E. J., Bland-Hawthorn, J., Castañeda, H. O., Gallego, J., González-Serrano, J. I., González, J. J., Jones, D. Heath, Pérez-García, A. M., Sánchez-Portal, M. 2005, *Rev. Mexicana Astron. Astrofis.*, 24, 82
- Coil, A. L., Newman, J. A., Kaiser, N., Davis, M., Ma, Ch., Kocevski, D. D., Koo, D. C. 2004, *ApJ*, 617, 765
- Conselice, C. J., 2003, *ApJS*, 147, 1
- de Ruitter, H. R., Willis, A. G. & Arp, H. C. 1977, *A&AS*, 28, 211

- Della Ceca, R., Maccacaro, T., Caccianiga, A., Severgnini, P., Braito, V., Barcons, X., Carrera, F. J., Watson, M. G., Tedds, J. A., Brunner, H. & 4 coauthors 2004, *A&A*, 428, 383
- Dickinson, M. et al. 2004, *ApJ*, 99, 122
- Ferrarese, L. & Merritt, D. 2000, *ApJ*, 539, L9
- Fiore, F., Elvis, M., Maiolino, R., Nicastro, F., Siemiginowska, A., Stratta, G., & D’Elia, V. 2003, *A&A*, 409, 57
- Fiore, F., Antonelli, L. A., Ciliegi, P., Comastri, A., Giommi, P., La Franca, F., Maiolino, R., Matt, G., Molendi, S., Perola, G. C., Vignali, C. 2001, *AIPC*, 599, 111
- Furusawa, H., et al. 2008, *ApJS*, 176, 1
- Gandhi, P., et al. 2006, *A&A*, 457, 393
- Gebhardt, K. et al. 2000, *ApJ*, 119, 1157
- Georgakakis, A. et al. 2006, *MNRAS*, 371, 221
- Georgakakis, A., et al. 2007, *ApJ*, 660, L15
- Giacconi, R., et al. 2002, *ApJS*, 139, 369
- Gilli, R., et al. 2003, *ApJ*, 592, 721
- Gilli, R., et al. 2005, *A&A*, 430, 811
- Graham, A. W., Trujillo, I., & Caon, N. 2001a, *AJ*, 122, 1707
- Graham, A., Erwin, P., Caon, N. & Trujillo, I. 2001b, *ApJ*, 563, L11
- Grogin, N. A., et al. 2003, *ApJ*, 595, 685
- Grogin, N. A., et al. 2005, *ApJ*, 627, L97
- Grupe, D., 2004, *AJ*, 127, 1799
- Hasan, P. 2007, *Ap&SS*, 312, 63
- Im, M., Simard, L., Faber, S. M., Koo, D. C., Gebhardt, K., Willmer, C. N. A., Phillips, A., Illingworth, G., Vogt, N. P., & Sarajedini, V. L. 2002, *ApJ*, 571, 171
- Kauffmann, G. et al. 2003, *MNRAS*, 346, 1055
- Kawakatu, N. et al. 2007, *ApJ*, 661, 660
- Laird, E.S., et al. 2008, *ApJS*, *submitted*
- Landy, S. D. & Szalay, A. S. 1993, *ApJ*, 412, 64
- Magorrian, J., et al. 1998, *AJ*, 115, 2285
- Manners, J. C., et al. 2003, *MNRAS*, 343, 293
- Mayer, L., Kazantzidis, S., Madau, P., Colpi, M., Quinn, T. & Wadsley, J. 2007, *Science*, 316, 1874
- Miyaji, T., et al. 2007, *ApJS*, 172, 396
- Mushotzky, R. 2004, *Supermassive Black Holes in the Distant Universe*, 308, 53
- Nandra, K., et al. 2005, *MNRAS*, 356, 568
- Peebles, P. J. E. 1980, *The Large Scale Structure of the Universe* (Princeton University Press)
- Puccetti, S., et al. 2006, *A&A*, 457, 501
- Sánchez-Portal, M., Díaz, A. I., Terlevich, E., & Terlevich, R. 2004, *MNRAS*, 350, 1087
- Sánchez-Portal, M., Pérez García, A. M., Cepa, J., González-Serrano, J. I., Alfaro, E. J., Castañeda, H. O., Gallego, J., González, J. J. 2007, *Rev. Mexicana Astron. Astrofis.*, 29, 175
- Schade, D., Lilly, S. J., Le Fevre, O., Hammer, F. & Crampton, D. 1996, *ApJ*, 464, 79S
- Schade, D., Lilly, S. J., Crampton, D., Hammer, F., Le Fevre, O. & Tresse, L. 1995, *ApJ*, 451, 1
- Shang, Z., Wills, B. J., Wills, D. & Brotherton, M. S., 2007, *AJ*, 134, 294S
- Shemmer, O., Brandt, W. N., Netzer, H., Maiolino, R., Kaspi, S. 2006, *ApJ*, 646, 29
- Simard, L., Willmer, C. N. A., Vogt, N. P., Sarajedini, V. L., Phillips, A. C., Weiner, B. J., Koo, D. C., Im, M., Illingworth, G. D., & Faber, S. M. 2002, *ApJS*, 142, 1S
- Simard, L. 1998, *ASPC*, 145, 108
- Steffen, A.T., Strateva, I., Brandt, N., Alexander, D. M., Koekemoer, A. M., Lehmer, B. D., Schneider, D. P. & Vignali, C., 2006, *AJ*, 131, 2826
- Stetson, P. B. 1987, *PASP*, 99, 191
- Taylor, M. B. 2005, *ASPC*, 347, 29

Ueda, Y., et al. 2008, ArXiv e-prints, 806,
arXiv:0806.2846

Waskett, T. J., Eales, S. A., Gear, W. K., Mc-
Cracken, H. J., Lilly, S., & Brodwin, M. 2005,
MNRAS, 363, 801

Wu, X. & Liu, F. K. 2004, ApJ, 614, 91

Yang, Y., Mushotzky, R. F., Barger, A. J., Cowie,
L. L., Sanders, D. B., & Steffen, A. T. 2003,
ApJ, 585, L85

Yang, Y., Mushotzky, R. F., Barger, A. J. &
Cowie, L. L. 2006, ApJ, 645, 68

Yee, H. K. 1983, ApJ, 272, 473

OTELO Survey: Deep BVRI broadband photometry of the Groth strip

II. Properties of X-ray Emitters

M. Pović

Instituto de Astrofísica de Canarias, 38205 La Laguna, Spain

`mpovic@iac.es`

M. Sánchez-Portal

Herschel Science Centre, ESAC/INSA, P.O. Box 78, 28691 Villanueva de la Cañada, Madrid, Spain

`miguel.sanchez@sciops.esa.int`

A. M. Pérez García

Instituto de Astrofísica de Canarias, 38205 La Laguna, Spain

A. Bongiovanni

Instituto de Astrofísica de Canarias, 38205 La Laguna, Spain

J. Cepa¹

Departamento de Astrofísica, Universidad de La Laguna, 38205 La Laguna, Spain

J.A. Acosta-Pulido

Instituto de Astrofísica de Canarias, 38205 La Laguna, Spain

E. Alfaro

Instituto de Astrofísica de Andalucía-CSIC, Granada, Spain

H. Castañeda

Instituto de Astrofísica de Canarias, 38205 La Laguna, Spain

M. Fernández Lorenzo

Instituto de Astrofísica de Canarias, 38205 La Laguna, Spain

J. Gallego

Departamento de Astrofísica y CC. de la Atmósfera, Universidad Complutense de Madrid, Madrid, Spain

J. I. González-Serrano

J. J. González

Instituto de Astronomía UNAM, México D.F, México

M. A. Lara-López

Instituto de Astrofísica de Canarias, 38205 La Laguna, Spain

ABSTRACT

The Groth field is one of the sky regions that will be targeted by the OTELO (OSIRIS Tunable Filter Emission Line Object) survey in the optical 820 nm and 920 nm atmospheric windows. This field has been observed by AEGIS (All-wavelength Extended Groth strip International Survey) covering the full spectral range, from X-rays to radio waves. *Chandra* X-ray data with total exposure time of 200ksec are analyzed and combined with optical broadband data of the Groth field in order to study a set of structural parameters of the X-ray emitters and its relation with X-ray properties. We processed the raw, public X-ray data using the *Chandra* Interactive Analysis of Observations and determined and analyzed different structural parameters in order to produce a morphological classification of X-ray sources. Finally, we analyzed the angular clustering of these sources using 2-point correlation functions. We present a catalog of 340 X-ray emitters with optical counterpart. We obtained the number counts and compared them with AEGIS data. Objects have been classified by nuclear type using a diagnostic diagram relating X-ray-to-optical ratio (X/O) to hardness ratio (HR). Also, we combined structural parameters with other X-ray and optical properties, and found for the first time an anticorrelation between the X/O ratio and the Abraham concentration index which might suggest that early type galaxies have lower Eddington rates than those of late type galaxies. A significant positive angular clustering was obtained from a preliminary analysis of 4 subsamples of the X-ray sources catalog. The clustering signal of the optically extended counterparts is similar to that of strongly clustered populations like red and very red galaxies, suggesting that the environment plays an important role in AGN phenomena.

Subject headings: Galaxies: active — X-rays: galaxies

1. Introduction

The OTELO project (Cepa et al. 2005, 2008) is a flux-limited survey of emission-line objects in large and perfectly defined volumes of the Universe. The OTELO survey, more than one magnitude deeper than other emission line surveys, includes a wide variety of astronomical sources: star-forming galaxies, starburst galaxies, emission-line ellipticals, AGNs, QSOs, Ly α emitters, peculiar stars, etc. With these data, a number of scientific problems will be addressed,

including: star formation rates (SFR) and metallicity evolution of galaxies; AGN and QSO evolution. Deep imaging programs such as several VLT surveys for GOODS (Dickinson et al. 2004), COSMOS (Capak et al. 2007) and SXDS (Furusawa et al. 2008) fields will serve as preparatory work for OTELO. Likewise, we have performed a deep BVRI broadband survey in one of the fields of the Groth strip selected for the OTELO survey (Cepa et al. 2008).

In the present work, data from this broad band survey is combined with other wavelength data

¹Instituto de Astrofísica de Canarias, 38205 La Laguna, Spain

for achieving several objectives of the OTELO project. Specifically, the matching of these optical data with X-ray allows successfully tackling the study of the AGN population as shown in Barcons et al. (2007), Georgakakis et al. (2006), and Steffen et al. (2006). Optical imaging surveys allow a morphological classification of all sufficiently resolved sources. This is essential to reveal the nature of AGN host galaxies (e.g. Hasan 2007; Fiore et al. 2001), although the morphological classification becomes difficult at high redshift, due to the reduced resolution of images. Several works (Graham et al. 2001b; Ferrarese & Merrit 2000; Gebhardt et al. 2000) have shown that the AGNs are directly related with some host galaxy properties, particularly with their bulges. Kauffmann et al. (2003) have pointed out that the AGNs in the local universe are hosted predominantly in bulge-dominated galaxies. More recently, Hasan (2007) using HST and *Chandra* data of the GOODS South field has found that the most moderate luminosity AGNs hosts are bulge-dominated in the redshift range $z \sim 0.4\text{--}1.3$. A tight correlation between black hole mass and the bulge dispersion velocity has been well established (Ferrarese & Merrit 2000; Gebhardt et al. 2000), as well as with the concentration of bulges (Graham et al. 2001b).

On the other hand, deep X-ray extragalactic surveys are extremely useful tools to investigate the time evolution of the population of active galactic nuclei (AGN) and to shed light on their triggering mechanisms. The exceptional effectiveness at finding AGN arises largely because X-ray selection has reduced absorption bias, minimal dilution by host-galaxy starlight and allows efficient optical spectroscopic follow-ups of high probability AGN candidates with faint optical counterparts. The *Chandra* and *XMM-Newton* observatories have revolutionized this field of research, generating the most sensitive X-ray surveys ever performed. In fact, deep surveys produced by these observatories have increased the resolved fraction of the cosmic X-ray background (CXRB) to about 90% in the 0.5–2 keV range. A large part of the detected X-ray sources are AGN ($\leq 70\%$), although X-ray emitters include a mix of different types of objects such as galaxy clusters and stars. On the other hand, these powerful observatories make it possible to access the hard (2–10 keV) range, allowing to directly probe the AGN activity not

contaminated by star formation processes. Moreover, hard X-ray surveys are capable to detect all but the most absorbed (Compton thick) sources. Therefore, they provide the most complete and unbiased samples of AGNs (Mushotzky 2004; Brandt & Hasinger 2005). Number counts relations have now been determined (e.g. Cappelluti et al. 2007) although with some evidence for field-to-field variations. Such variations are expected at some level owing to "cosmic statistics" associated with large-scale structures and clustering features that have been detected in the X-ray sky (Barger et al. 2003; Yang et al. 2003; Gilli et al. 2003, 2005).

In this paper we present the analysis of public, deep (200 ksec) *Chandra*/ACIS observations of three fields comprising the original Groth-Westphal strip (GWS), gathered from the *Chandra* Data Archive, and combined with optical BVRI data from our broadband survey carried out with the 4.2m William-Herschel Telescope (WHT) at La Palma (see Cepa et al. 2008, for a detailed description). We have tried to implement an innovative approach to the optical study of X-ray emitters by investigating correlations between broadband optical and X-ray parameters, specifically the X-ray-to-optical ratio and hardness ratios, and optical structural parameters that provide information about the host galaxy morphology and populations, like asymmetry and concentration indexes and optical colors.

This paper is structured as follows: in Section 2, we describe the observational data, including X-ray data processing and source detection, as well as optical broadband data and the selection of the sample of X-ray sources with optical counterparts. Section 3 reviews the X-ray properties of the galaxy sample, the procedures for computing optical structural parameters, as well as the morphological analysis carried out. The reliability of different structural parameters used in morphological classification is also discussed. Section 4 presents the nuclear type classification, the relationship between X-ray and optical structural properties, and the comparison with results from the literature. The catalog of X-ray emitters with optical counterparts and their morphological classification is presented in the electronic edition. Finally, in Section 5 we present the results of the clustering analysis (based on the angular correlation function formalism) applied on 4 selected

subsamples of the X-ray catalog.

2. Observational data

2.1. X-ray data

2.1.1. Observations and data processing

Chandra has observed three consecutive fields centered at the original HST Groth-Westphal strip (GWS) using the ACIS-I instrument. All datasets have been gathered from the *Chandra* Data Archive (<http://asc.harvard.edu/cda/>) using the Chaser tool. PI of all the retrieved *Chandra* observations is K. Nandra. Total exposure time in each field is about 200 ksec. The total field size of ACIS-I chips 0, 1, 2 & 3 is $16.9' \times 16.9'$ (ACIS-S chips 2 & 3 were also used, but their FOVs do not overlap with our optical data and therefore were not used). The FAINT and VFAINT telemetry modes have been used, with telemetry saturation rates of 170 and 67 events/s, respectively. Due to the lack of bright sources within the fields, we assume that there are no pile-up effects in any observation. Table 1 summarizes the main characteristics of the *Chandra* observations.

We processed the data Using the *Chandra* Interactive Analysis of Observations (CIAO) (<http://cxc.harvard.edu/ciao/>), v4.0 and Calibration Data Base (CALDB) v3.4.0. Standard reduction procedures have been applied, as described in the CIAO Science Threads to produce new level 2 event files. The output level 2 event files have been restricted to the 0.5–8 keV range to avoid high background spectral regions. Furthermore, we analyzed the source-free light curves in order to define additional good time intervals (GTI). To this end, we applied the CIAO detection program `celldetect` with a threshold $S/N=3$. The detected sources have been removed upon creation of the time-binned light curves, that have been then used for the computation of the GTIs. A $\pm 3\sigma$ rejection criterion has been applied to remove high background intervals. After filtering for the additional GTIs, the level 2 event files belonging to the same target were co-added. To this end, we first improved the absolute astrometry (the overall 90% uncertainty circle of *Chandra* X-ray absolute position has a radius of 0.6 arcsec) applying corrections for translation, scale and rotation to the world coordinate system (WCS) of

Table 1: *Chandra* observations log for the three pointings of the GWS field. Col. (1): observation number; Col. (2,3): RA and DEC (J2000); Col. (4): Standard Data Processing (SDP) version; Col. (5): Observation format in the Time exposure mode; Col. (6): Net exposure time (Sum of Good Time Intervals, GTI) (ksec)

Obs (1)	RA (2)	DEC (3)	SDP (4)	Mode (5)	GTI (6)
5853	14:15:22.5	+52:08:26.4	7.6.7.1	VFAINT	42.4
5854			7.6.7.1	VFAINT	50.2
6222			7.6.7.1	VFAINT	35.2
6223			7.6.7.1	VFAINT	49
6366			7.6.7.1	VFAINT	15.96
7187			7.6.7.1	VFAINT	8
5851	14:16:24.5	+52:20:02.59	7.6.7.1	VFAINT	36
5852			7.6.4	VFAINT	11.95
6220			7.6.7.1	VFAINT	36
6221			7.6.7.1	VFAINT	3.8
6391			7.6.7.1	VFAINT	9.4
7169			7.6.4.1	VFAINT	18.2
7181			7.6.7.1	VFAINT	8
7188			7.6.4.1	VFAINT	4.2
7236			7.6.4	VFAINT	18.8
7237			7.6.4.1	VFAINT	17.2
7238			7.6.4	VFAINT	9.6
7239			7.6.4.1	VFAINT	16.2
3305	14:17:43.0	+52:28:25.2	6.8.0	FAINT	27.6
4357			6.9.0	FAINT	79.8
4365			6.9.0	FAINT	58.2

each data file, by comparing two sets of source lists from the same sky region. Average positional accuracy improvement is 6.3% with respect to the original astrometry provided by the spacecraft attitude files. Once we have improved the astrometry, the event files have been merged.

The output merged files have been filtered to create event files for several energy bands: full (0.5–7 keV), soft (0.5–2 keV), hard (2–7 keV) hard2 (2–4.5 keV) and vhard (4–7 keV). Unbinned effective exposure maps at a single energy, representative of each band, were created at 2.5 keV (full), 1 keV (soft), 4 keV (hard), 3 keV (hard2) and 5.5 keV (vhard). Resulting maps have units of time \times effective area, i.e. $\text{s cm}^2 \text{ counts photon}^{-1}$.

2.1.2. Source detection

We applied the CIAO `wavdetect` Mexican-Hat wavelet source detection¹ program to all bands (full, soft, hard, hard2 and vhard) for the three fields. Several wavelet scales have been applied: 1, $\sqrt{2}$, 2, $2\sqrt{2}$, 4, $4\sqrt{2}$, 8, $8\sqrt{2}$ and 16 pixels. Small scales are well suited to the detection of small sources while larger scales are appropriate for more extended sources. Due to the “blank field” nature of the GWS, we do not expect to detect sources at a scale larger than 16 pixels (~ 8 arcsec). For each applied scale, `wtransform` produces a complete set of detections. We set a significance threshold of 2×10^{-7} . Since this `wavdetect` input parameter measures the number of spurious events per pixel, we expect ≈ 0.2 fake detections per detector of 1024×1024 pixels i.e. about 12 spurious sources in the entire catalog (4 detectors \times 5 bands \times 3 fields). The output `wavdetect` detection files are FITS tables containing the position of sources (RA & DEC), count rates in photons $\text{s}^{-1} \text{cm}^{-2}$ and ancillary information. The final X-ray source catalog has been obtained by cross-matching detections in all five bands in order to increase the reliability of detections. Best match is given by a minimum separation of sources around a great circle. We set a maximum search distance of 2 arcsec (see section 2.4). We computed the hardness ratios as follows:

$$HR(\Delta_1 E, \Delta_2 E) = \frac{CR(\Delta_1 E) - CR(\Delta_2 E)}{CR(\Delta_1 E) + CR(\Delta_2 E)} \quad (1)$$

where $\Delta_1 E$ y $\Delta_2 E$ are different energy bands and $CR(\Delta_n E)$ is the count rate in a given energy band. Four hardness ratios have been set in this way: $HR_1 \equiv HR(\text{hard}, \text{soft})$, $HR'_1 \equiv HR(\text{hard2}, \text{soft})$, $HR_2 \equiv HR(\text{very hard}, \text{hard})$ and $HR'_2 \equiv HR(\text{very hard}, \text{hard2})$.

We also computed the energetic fluxes from count rates. To this end, mean photon energies in each band have been calculated assuming a power law spectrum with $\Gamma = 1.5$ (a reasonable assumption after inspecting the hardness ratios diagram and diagnosis grid depicted in Figure 5), redshift $z = 0.5$, galactic absorption $n_H = 1.3 \times 10^{20} \text{cm}^{-2}$

and no intrinsic absorption. We applied the absorption coefficients provided by the `TRANNM` function within the package `PIMMS v3.9b` (Mukai, 1993). The output catalog has 639 unique X-ray emitters (after removing 20 common sources in the field overlapping area). From them, 76 objects are located outside the field covered by optical data. From the total sources, 46% (297) have been detected with a significance $\geq 4\sigma$, 21% (132) above the 3σ significance level and 13% (81) down to 2.5σ level.

The number of sources detected in each band are 490 (full), 465 (soft), 284 (hard), 266 (hard2) and 121 (vhhard), with median fluxes of 1.81×10^{-15} , 5.57×10^{-16} , 2.34×10^{-15} , 1.58×10^{-15} and $3.75 \times 10^{-15} \text{erg cm}^{-2} \text{s}^{-1}$, and with limiting fluxes at 3σ level of 4.8×10^{-16} , 1.1×10^{-16} , 2.8×10^{-16} , 1.3×10^{-16} and $7.3 \times 10^{-16} \text{erg cm}^{-2} \text{s}^{-1}$, respectively. Median errors in fluxes (for objects above the 3σ significance level) are 8% in full band, 10% in soft band, 12% in hard band, 14% in hard2 band and 22% in vhard band. There are 16 sources detected only in hard band, 18 in hard2 band and 3 sources are only observed in vhard band. We find an overabundance of soft X-ray sources in our final catalog. There are 103 sources detected only in this band. This effect can be at least partially explained considering the decrease of telescope + ACIS effective area from some 600cm^2 in the 1–2 keV range (including the 0.5–2 keV band defined as soft), until approximately 200cm^2 at ~ 6 keV. On the other hand, the total background between 0.5 and 7 keV is around 4 times higher than in the 0.5–2 keV range. The combination of these two factors justifies the high *Chandra*/ACIS source detection efficiency in the soft X-ray band and the mentioned overabundance. The first version of this catalog was presented in Sánchez-Portal et al. (2007).

2.2. Comparison with AEGIS data

The All-wavelength Extended Groth strip International Survey (AEGIS) collaboration has recently made public their data sets, including a catalog of X-ray sources that comprises the observations used within this paper. The complete AEGIS X-ray catalog (Laird et al. 2008) consists of 1325 sources; from these, 471 are located within the area covered by our data (fields EGS-6, 7 and

¹The fact that the PSF of X-ray detectors often has Gaussian-like shape motivates our use of the Marr wavelet, or “Mexican Hat” function.

8 according to their nomenclature). From our 429 sources detected above 3σ significance level, 416 coincide with AEGIS sources using a search radius of 2 arcsec (388 sources if only unique matches are considered). Figure 1 shows a good agreement between the source counts used in this work and those provided by the AEGIS team: median relative deviations of our data with respect to AEGIS are 2% (full band), 0.7% (soft), 5.5% (hard) and 7.8% (vhard).

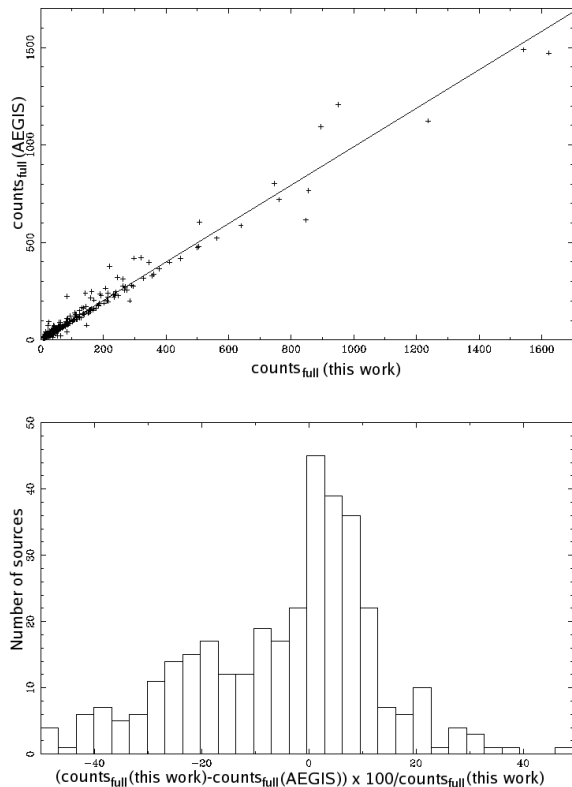


Fig. 1.— Upper panel: full band net counts from this work vs AEGIS net counts. The solid line represents the best linear fit, with a slope of 0.99 and zero point 5.23 counts. Lower panel: histogram of relative deviations of our full band count data with respect to AEGIS. Median deviation is lower than 2%.

2.3. Optical data

We observed three pointings in the direction of the GWS, each of them using the B, V, R, and I broadband filters. The total area covered is 0.18 square degrees. The observations have been car-

ried out using the Prime Focus Imaging Platform (PFIP) at the 4.2m William-Herschel Telescope (WHT) in the Roque de los Muchachos Observatory (La Palma, Canary Islands). This camera has two CCD detectors ($2k \times 4k$), with a total field of view of $16' \times 16'$ and a pixel size of 0.237 arcsec. Several exposures have been performed at each pointing, of 600, 800, 900, or 1000 sec, depending on the filter, with a dithering of 15 arcsec between consecutive exposures in order to allow eliminating cosmic rays and to fill the gap between detectors. Standard reduction procedures have been applied. Resulting limiting magnitudes are 25, 25, 24.5 and 23.5 in B, V, R and I band, respectively. A detailed description of data reduction and optical source detection can be found in Cepa et al. (2008). The optical catalog used in this work contains data for ~ 44000 objects.

2.4. The catalog of optical counterparts

In order to build a sample of X-ray emitters with optical counterparts, we performed cross-matching of the X-ray and optical catalogs using the TOPCAT tool (Taylor 2005), applying a criterion of minimum sky distance along a great circle. X-ray sources located inside the field covered by optical data and their optical counterparts are represented in Figure 2.

We chose a maximum search radius of 2 arcsec after carrying out several tests considering a maximum searching distance of 1 to 5 arcsec with a bin of 0.5 arcsec (Figure 3). As expected, the number of counterparts increases with the maximum search radius, but also the number of multiple matches within the error circle. Setting a search radius of 1 arcsec we minimise the number of multiple cross-matches, but at the cost of losing an outstanding number of potential counterparts. On the other hand, choosing a search radius greater than 2 arcsec produces a large number of multiple matches, increasing the uncertainty in counterpart identification. Therefore, we set a 2 arcsec search radius as an adequate compromise. This practical criterion is consistent with the more rigorous analysis performed below.

We detected 340 optical counterparts of the X-ray sources in at least one optical band. Of them, 322 are detected in the B band, 332 in V, 334 in R and 317 in the I band.

We carried out a quantitative analysis of

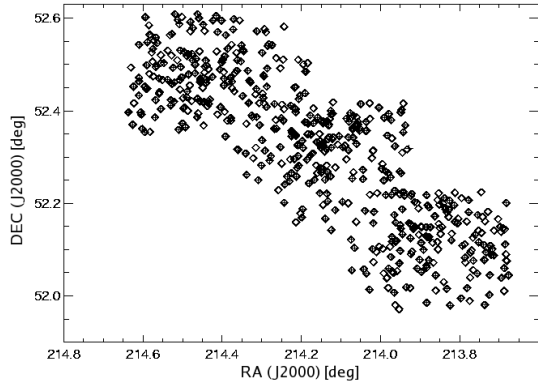


Fig. 2.— X-ray sources (diamonds) and their optical counterparts (filled diamonds) from the cross-match of X-ray and optical catalogs

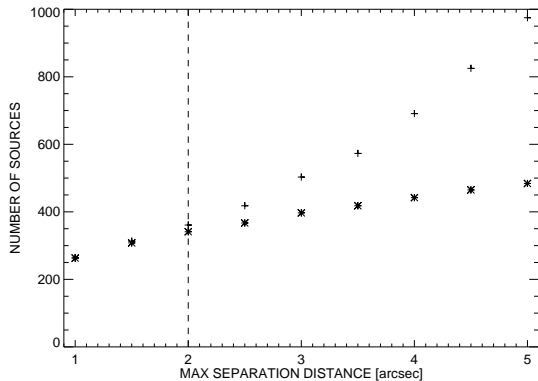


Fig. 3.— Number of optical counterparts as a function of the maximum search radius used for cross-matching. The number of closest sources is represented with stars. Crosses represent the total number of sources found within the search radius. The dashed line marks the adopted separation. The same value was obtained applying the statistical methodology of de Ruiter et al. (1977)

the completeness¹ and reliability² of our cross-matching procedure by applying the methodology of de Ruiter et al. (1977). The separation between sources is defined by the dimensionless variable r as:

¹Fraction of all real associations between the X-ray and optical sources that are indeed classified as identifications.

²Fraction of claimed identifications expected to be true counterparts.

$$r = \left(\frac{\Delta\alpha^2}{\sigma_\alpha^2} + \frac{\Delta\delta^2}{\sigma_\delta^2} \right)^{1/2}, \quad (2)$$

where $\Delta\alpha$ and $\Delta\delta$ are the position differences between the X-ray source and its optical counterpart in RA & DEC, and σ_α^2 and σ_δ^2 are the overall astrometric errors computed as $\sigma = (\sigma_X^2 + \sigma_{opt}^2)^{1/2}$. In this work, we assume $\sigma_X = 0.7$ arcsec and $\sigma_{opt} = 0.3$ arcsec. σ_X was calculated by square adding a systematic uncertainty of 0.5 and a centroiding error of 0.5 arcsec.

The likelihood ratio is defined as:

$$LR(r) = \frac{dp(r|id)}{dp(r|c)} = \frac{1}{2\lambda} e^{\frac{r^2}{2}(2\lambda-1)} \quad (3)$$

where:

- $dp(r|id)$ is the *a priori* probability that an X-ray source and its optical counterpart have a separation between r , and $r + dr$ due to astrometrical errors
- $dp(r|c)$ is the probability that a confusing background optical object is found in the range r , and $r + dr$ from the X-ray source position.
- λ measures the number of confusing objects within the error circle and depends on the optical objects density (ρ_{opt}) as: $\lambda = \pi\sigma_\alpha\sigma_\delta\rho_{opt}$.

An optical source can be considered as a true counterpart of an X-ray source if its LR is higher than a certain threshold value L . L is obtained maximising the sum of completeness and reliability that are, in turn, mathematically defined in terms of the probabilities defined above. In our case, $L = 0.56$ and its corresponding variable is $r = 2.6$ which gives us a separation distance of 2.0 arcsec, a value consistent with the adopted one. The completeness of our detection is 98.3% (i.e. some 1 object lost due to the use of a particular cutoff value L), while reliability is 87.3% (~ 39 potentially false matchings).

3. Analysis

3.1. X-ray properties

We have computed the cumulative number count distributions ($\log N$ - $\log S$) per deg^2 in the soft band and compared it with other surveys in order to check the reliability of our source detections. We have chosen the soft band to be able to compare our distribution with that computed by Nandra et al. (2005) and those provided by other deep X-ray surveys, Chandra Deep Field South (CDFS, Giacconi et al. 2002), Chandra Deep Field North (CDFN, Alexander et al. 2003), ELAIS-N1 and ELAIS-N2 (Manners et al. 2003). All distributions are represented in Figure 4. For our sample two curves have been computed, one for the complete sample of X-ray detections and the other only for the X-ray detections that have optical counterparts. The median flux levels are 1.81×10^{-15} and $1.97 \times 10^{-15} \text{ erg cm}^{-2} \text{ s}^{-1}$, respectively. For the objects brighter than $\sim 10^{-14} \text{ erg s}^{-1} \text{ cm}^{-2}$ both distributions coincide, while for objects fainter than $\sim 10^{-14} \text{ erg s}^{-1} \text{ cm}^{-2}$ the density of X-ray sources with optical counterparts starts to decrease, since the optical sample is incomplete at the depth of our X-ray data. In general, at our flux limit the number counts of our complete X-ray sample are in good agreement with Nandra et al. (2005) and other surveys. We have detected a higher density of sources with flux below $\sim 5 \times 10^{-15} \text{ erg cm}^{-2} \text{ s}^{-1}$, most likely due to the use of different detection algorithms and more sensitive detection threshold. As we already mentioned, our threshold is 2×10^{-7} , two times higher than the one chosen by Nandra et al. (2005) (see 2.1.2 for more information).

Three independent energy bands, soft, hard2 and vhard (see the Section 2.1.1 for ranges), have been used to obtain the X-ray color-color diagram shown in Figure 5. Hardness ratios have been calculated as described in Section 2.1.2. X-ray sources are superimposed on a model grid computed using power law Spectral Energy Distributions (SEDs) with different photon indexes, Γ , affected by a galactic absorption column density, N_H , of $1.3 \times 10^{20} \text{ cm}^{-2}$ and different values of intrinsic absorption; the *Chandra* ACIS-I response matrices have been also included in the computation. To obtain the fluxes we have used XSPEC

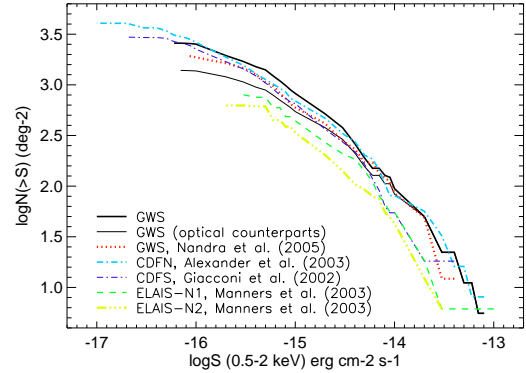


Fig. 4.— Cumulative $\log N$ - $\log S$ functions for the Groth field in the soft band, for all detected X-ray sources (thick solid line) and for X-ray sources with optical counterpart (thin solid line). Five distributions, with different exposure times and effective areas, have also been represented as comparison: GWS by Nandra et al. (2005) (dotted line), CDFN (thick dash-dot-dash line), CDFS (thin dash-dot-dash line), ELAIS-N1 (dash line) and ELAIS-N2 (dash-dot-dot-dash line)

(Arnaud 1996), varying the photon index between 0 and 3 with a step size of 0.5, and the intrinsic absorption column density between 20 and 24 (in logarithmic scale) in steps of 0.5. The majority of our sources are located within the model grid region, suggesting that their X-ray SED is compatible with the assumed model. A specially high concentration of objects can be seen in the region of N_H between 10^{20} and $5 \times 10^{21} \text{ cm}^{-2}$ and with $\Gamma \simeq 1.8$. A group of sources are located outside the model grid, showing a soft excess, suggesting that they can not be properly described by a single power law. For the fitting of these objects probably more components should be added.

3.2. Optical structural parameters

We obtained a set of structural parameters of the optical counterparts of our X-ray sample, in order to describe quantitatively their structure and morphology. In this section we describe the procedure used to derive the parameters and to produce a morphological classification.

We used SExtractor v2.2.2 (Bertin & Arnouts 1996) to detect and extract the sources. Details

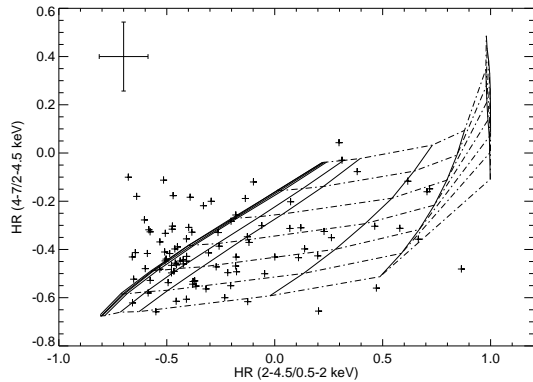


Fig. 5.— X-ray color-color diagram based on 2–4.5/0.5–2keV (HR'_1) vs. 4–7/2–4.5keV (HR'_2) hardness ratios. X-ray sources (crosses), from the complete X-ray catalog, are represented and superposed on an absorbed power law model grid. Photon index is varying between 0 and 3 in steps of 0.5 (dashed lines from up to down) and a $\log(N_H)$ between 20 and 24 in steps of 0.5 (solid lines from left to right). Median error bars are represented in the upper left corner of the diagram.

of the source extraction process are provided in Cepa et al. (2008). The version used (v2.2.2) was modified by B. Holwerda to measure the Abraham concentration index (Abraham et al. 1994). This is defined as the ratio between the integrated flux within certain radius defined by the normalized radius α and the total flux. We used the values obtained at $\alpha=0.3$ in our analysis in order to compare our results with those of Abraham et al. (1996). Another relevant output parameters for our study are the CLASS_STAR, which permits to roughly classify objects as compact or extended (for more information see Section 3.2.1), and the background that will be used later.

In addition, we used the Galaxy Image 2D software package (GIM2D, Simard 1998; Simard et al. 2002) versions 2.2.1 and 3.1, to perform the galaxy structural parameter decomposition (see Figure 6). This software considers two components: an spheroid, represented by a Sérsic profile², and a disk represented by an exponential profile. Using the standard steps in DAOPHOT

²While any rigorous analysis of the structural components of an AGN host should include an additional component, namely a pointlike nucleus, the small size of most of our

(Stetson 1987) we obtained the PSF images required for GIM2D execution. The initial parameters (including background estimation) and setup for GIM2D were determined using the images and catalogs produced by SExtractor (Bertin & Arnouts 1996). We obtained from the output provided by GIM2D the following parameters³: bulge-to-total ratio (B/T), residual parameter (R) (Schade et al. 1995, 1996), asymmetry (A) index (Abraham et al. 1994, 1996), the Sérsic index (n) and the total luminosity (L_{tot}). The residual parameter and the asymmetry index quantify the galaxy irregularity, by measuring the deviation from the simple, symmetric model (e.g. spheroid + disk), using as input the residual and original image, respectively. GIM2D also calculates for certain output parameters their lower and upper limits at 99% confidence level. In order to estimate the accuracy of the best fit parameters we have looked at the deviation, computed as the maximum between the best value and the upper or lower limits (see Figure 7). In this respect, the B/T parameter and Sérsic index have revealed inaccurate when applied to faint and small objects ($\lesssim 300$ pixel, while the seeing disk (FWHM) area is about 30 pixels) as shown in Figure 7. Therefore we have decided to do not use these parameters for the morphological classification.

In practice, we observed that the code either fails or produces unreliable output parameters in a number of cases: (1) when the source R magnitude is less than 18 or larger than 24, (2) when the isophotal area is very small (usually less than 90 pixels), (3) when the central object is surrounded by close neighbouring sources or nearby bright companions, and (4) when the source is close to the frame boundaries.

objects compared with the seeing disk prevents from implementing such a detailed approach. Rather, we have simply assumed that the sum of the nuclear and bulge components can be roughly represented by a single Sérsic profile.

³According to the available documentation (Simard 1998; Simard et al. 2002), GIM2D calculates the Abraham concentration at four normalized radii $\alpha = 0.1, 0.2, 0.3$ and 0.4 . (Abraham et al. 1994, 1996). Comparing the results with the ones obtained with SExtractor, a systematic shift of ~ 0.2 is found towards larger values in GIM2D figures. After performing several tests we concluded that the GIM2D code performs its computations using normalized area rather than normalized radius against what is stated in the documentation.

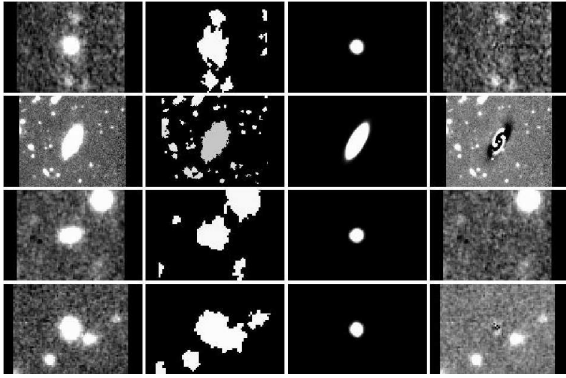


Fig. 6.— Four sample images of the GIM2D decomposition procedure. First column shows subimages (obtained from the scientific image) of objects to be fitted; the second column represents the mask subimages, third column shows the subimages obtained from the modelling and the fourth column shows the residual images, obtained from the original image after subtracting the model

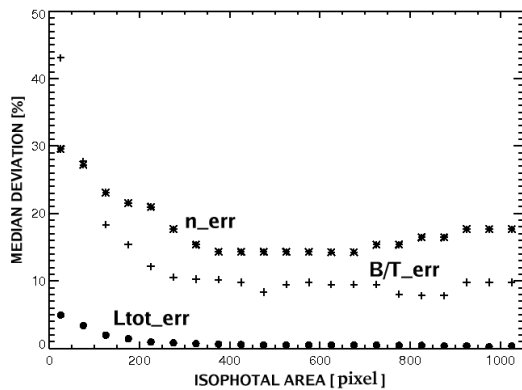


Fig. 7.— Evolution of the median error of the bulge-to-total ratio B/T (crosses), Sérsic index n (stars) and total flux (filled circles) L_{tot} as functions of the isophotal area. Deviations are evaluated as explained in Section 3.2.

3.2.1. Morphological classification

The selection of compact objects (QSOs, faint host AGNs or active stars) has been accomplished by using the SExtractor CLASS_STAR output parameter. The computed value depends on the seeing, the peak intensity of the source and its isophotal area. The parameter ranges between 0

(extended object like a galaxy) and 1 (pointlike object). A source has been deemed as compact if its CLASS_STAR parameter is larger than 0.9.

To determine the morphology of extended objects (i.e. not selected as compact according to the criterion above), we analyzed four parameters: Abraham concentration index (C), Abraham asymmetry index (A), B/T ratio and residual parameter (R). We carried out the analysis in three different bands (B, V, and R) in order to determine the most reliable parameters, and the best band for morphological classification. We excluded I band here due to fringing.

We first classified each object using the set of parameters mentioned above, separately for each parameter in each band, considering the results from previous works as limits between different morphological types. We used the results of Im et al. (2002) and Simard (1998) to obtain preliminary morphology with the B/T parameter, Schade et al. (1995) results for the residual parameter and Abraham et al. (1996) for the classification with the concentration and asymmetry index. In practice, we found that, in many cases, different parameter sets lead to a different classification of a given object even in the same band. In order to have an independent evaluation criterion, we also carried out a visual classification of the objects. Despite its subjectiveness, this procedure can yield highest-quality results when applied to bright and extended objects, thus being a convenient method to test the reliability of the structural parameters that will be in turn applied to the analysis of fainter objects. The visual classification has been accomplished by inspection of the radial profile, 2D surface plot and isophotal contours diagram of each source (see Figure 8). For the dimmest and smallest objects of our sample (galaxies with the magnitude $R > 24$ and isophotal area < 100 pixels) the profiles and isophotal contours are too noisy to get an acceptable result by means of a simple visual inspection.

From this comparison we conclude that for our sample, characterised by faint objects (typically $R \gtrsim 22$) with small isophotal area ($\lesssim 300$ pixel, while the seeing FWHM disk area is about 30 pixels) the most reliable parameter is the concentration index C , combined either with the asymmetry index or the residual parameter. We therefore based our morphological classification in the concentration

index combined with both asymmetry index and residual parameter. The R band has been used, since, on the one hand, the largest part of optical counterparts have been found in this band, and on the other, the achieved S/N is generally larger. B, V, and I bands have been used to perform the morphological classification of objects not detected in the R band, or detected in this band but with very low S/N ratio.

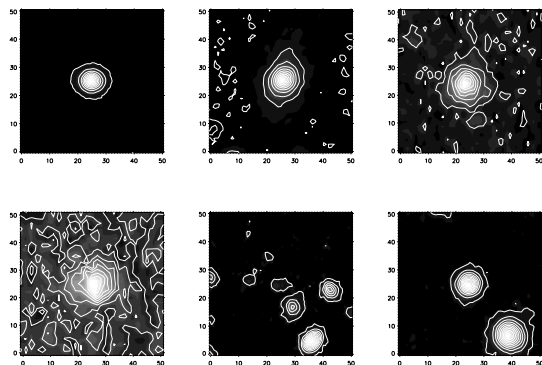


Fig. 8.— Sample of different Hubble type galaxies and their contour diagrams; Up: Left: Group I (E/S0), Center: group II (Early type spiral), Right: group III (Spiral); Down: Left, group III (Spiral), Center: group IV (Irr), Right: compact object ($C \geq 0.7$ or $\text{CLASS_STAR} > 0.9$). All objects are located in the center of the images.

Based on the classification using visual inspection of the brightest sample objects, and upon comparison with previous works (e.g. Abraham et al. 1996, see references above) in the present paper we created five categories or groups associating ranges of values of C with Hubble types:

- 0: $C \geq 0.7$ or $\text{CLASS_STAR} \geq 0.9 \rightarrow$ Compact obj.
- I: $0.45 \leq C < 0.7 \rightarrow$ E, E/S0 and S0
- II: $0.3 \leq C < 0.45 \rightarrow$ S0/S0a-Sa
- III: $0.15 \leq C < 0.3 \rightarrow$ Sab-Scd
- IV: $C < 0.15 \rightarrow$ Sdm-Irr

The first group is populated by elliptical and lenticular galaxies, whose profiles do not show any trace of disk or spiral arms (see Figure 8), the second group includes very early spiral type galaxies which show signs of spiral arms. The third

group comprises spiral galaxies while the fourth includes late type spirals and irregular galaxies, that show almost no regular form in their profiles. All galaxies, even those in the first group (elliptical and lenticular) have a concentration index $C \leq 0.7$, while all objects with $C > 0.7$ have been classified by SExtractor as compact ones, with the CLASS_STAR parameter > 0.9 .

In Figure 9 we depict the Abraham asymmetry vs. concentration index diagram segregated according to the morphology determined using the visual classification for the brightest objects, and the structural parameters (in most of the cases C combined with A) for the fainter ones. Comparing our Figure 9 with that shown in Abraham et al. (1996), it can be seen that in our case there is a small shift of the concentration index towards smaller values. This can be explained considering the influence of the atmospheric seeing conditions. SExtractor does not apply any correction on the computed parameters for this effect, and as the seeing induced PSF increases, both concentration and asymmetry indexes tend to decrease, as confirmed by our simulations carried out by convolving simple galaxy models with seeing PSFs of different widths. Since the Abraham et al. (1996) diagram has been obtained from HST data, these differences are expected.

The morphological analysis described above has been applied to the complete sample of 340 X-ray objects with optical counterpart (see Figure 10). Of those, 333 were classified using the R band, 4 sources using the V band and finally 3 objects by means of B band data. The largest group (143 sources) is composed by compact objects (QSOs, faint host AGNs, stars) followed by group III (73 galaxies). 57 objects are found either in group II or III, having outstanding bulge component a signs of a formed disk and spiral arms. Only 33 galaxies are found to belong to the IV group. Finally, we detected 7 closed pairs, whose possible physical relation will be confirmed when photometric redshifts are computed (paper III, in preparation). Due to the high noise level, or to the presence of other objects close to the observed ones, the classification uncertainty for some of the objects is quite high, and it was not possible to determine the morphological group: 3 galaxies could be either in group II or III and other 3 either in group

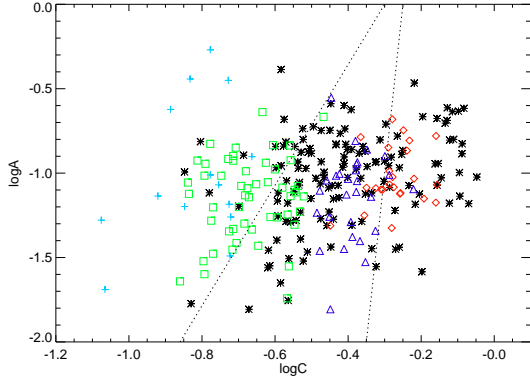


Fig. 9.— Morphological classification diagram combining the Abraham asymmetry index (A) vs. Abraham concentration index (C). Diamonds present E and S0 galaxies, triangles S0/S0a-Sa galaxies, squares young spiral galaxies (Sab-Sbcd) and crosses late type galaxies (Sdm-Irr). Compact objects are represented by star symbols. Dotted lines separate the loci of elliptical, spiral and peculiar galaxies (from right to left) obtained by Abraham et al. (1996). There is a small shift of our concentration and asymmetry index towards smaller values due to the influence of the atmospheric seeing conditions.

III or IV. For 21 sources it was not possible to determine the morphology since they are at the detection limit.

4. Relationship between X-ray and optical structural properties

4.1. Nuclear classification

The simplest way to classify the nuclear type is based on the X-ray-to-optical ratio (X/O). The typical value of X/O flux ratios for X-ray selected AGN (both type 1 or BLAGN and type 2 or NLAGN) is in the range between 0.1 and 10 (e.g. Fiore et al. 2003). For optically selected type 1 AGNs the typical value is $X/O \simeq 1$ (Alexander et al. 2001; Fiore et al. 2003). At high X/O flux ratios (well above 10) we can find BLAGN and NLAGN as well as high-z high-luminosity obscured AGN (type 2 QSOs), high-z clusters of galaxies and extreme BL Lac objects. Finally, the $X/O < 0.1$ region is typically populated by coronal emitting stars, normal galaxies (both early type

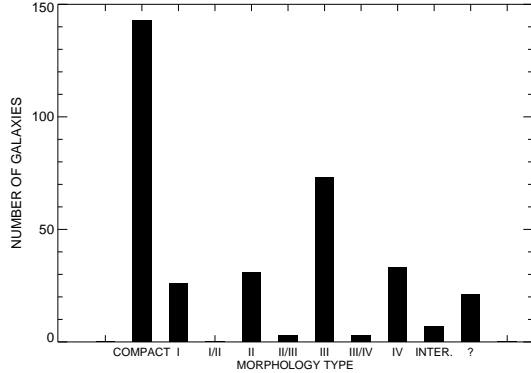


Fig. 10.— The histogram represents the final morphological classification of the GWS X-ray emitters with optical counterparts. Different values of the Abraham concentration index correspond to different groups I-IV (see text). A group of possible interacting objects has been detected; a group of sources (marked with '?') remained unidentified due to their very low S/N ratio.

and star-forming) and nearby heavily absorbed (Compton thick) AGN.

We have applied a simple criterion for performing a coarse nuclear-type classification of our sample objects, based on diagnostic diagrams relating X-ray-to-optical ratios (X/O) to hardness ratios (HR). This criterion is based on the results of Della Ceca et al. (2004) on the *XMM-Newton* Bright Serendipitous Survey; they found that, when plotting the $HR(2 - 4.5keV/0.5 - 2keV)$ (equivalent to our HR'_1) against X/O, computed as the ratio of the observed X-ray flux in the 0.5-4.5keV (soft+hard2) energy range and the optical R-band flux, most (85%) of the BLAGN identified by means of optical spectroscopy are tightly packed in a small rectangular region of the diagram, while NLAGN (type 2) tend to populate a wide area of the diagram (towards harder values of the hardness ratio). We applied the same approach to our sample, combining the HR'_1 hardness ratio with the X/O ratio, where the optical flux F_R has been derived from the Petrosian magnitudes in the R band. The resulting diagram, that also includes host morphology information, is shown in Figure 11, where the dashed-line box indicates the locus of the BLAGN region. We set the right edge of this box, $HR(2 - 4.5keV/0.5 - 2keV) \approx -0.35$ as

a coarse boundary separating 'unobscured' AGN (BLAGN) and 'obscured' AGN (NLAGN). On the other hand, we consider the small box depicted in the diagram as the "highest probability" region for finding a BLAGN (Della Ceca et al. 2004). We find that a large fraction of our objects, 63%⁴, fall inside the region of BLAGNs, while 51% of the sample is placed within the small BLAGN box defined by Della Ceca et al. (2004). Regarding morphology, we do not find evidence of any relationship between nuclear and morphological types, since we did not obtain any clear separation of nuclear species based on morphological type. Nevertheless, we can see that the majority of objects identified as compact (65%) are placed in the BLAGN region. It is also interesting to highlight the relationship between the X/O ratio and the host galaxy morphology, with early-type galaxies having generally lower values for X/O ratio and an opposite behavior of late-type objects. Finally, we find that only about 7% of our sample objects are placed in the lower region of the diagram (i.e. that typical of stars/normal galaxies/Compton-thick AGN).

We also represented the X/O ratio with respect to HR_1 , yielding a basically identical distribution as that described above, and with respect to HR_2 and HR'_2 , observing that in these two cases is harder to get a clear separation between different nuclear/morphological types; this behavior is expected since hardness ratios computed from the hard and vhard bands are less sensitive to absorption than those involving the soft band, which is one of the main criteria for the separation between broad and narrow line AGN.

4.2. X-ray and optical properties

We combined the X/O ratio with optical colors (B-R and B-I) for the different morphological groups and nuclear types, as shown in Figure 12. We observe that compact and late-type objects tend to show bluer colors, while early-type galaxies tend to present redder colors and also lower X/O values, as expected. On the other hand, there is a mild tendency for BLAGN to show

bluer colors than those found in NLAGN, as already observed in local universe samples (e.g. Yee 1983; Sánchez-Portal et al. 2004). The B-R average value for BLAGNs is 1.0 and for NLAGNs 1.4, with $\sigma=0.5$ and 0.6 respectively. Using the Kolmogorov-Smirnov test, the two distributions are statistically different with a significance level of 99%.

When representing the X/O ratio vs. the Abraham concentration index C we find a strong anticorrelation between these two parameters (Figure 13), obtaining a correlation coefficient of ~ -0.5 . Using Spearman and Kendall (S-K) statistics, we obtained a correlation significance level $>99\%$. The first order polynomial function has been fitted with a slope of -2.03, log X/O-intercept of -0.94 and a standard deviation of ~ 0.5 . This result is consistent with that referred above and depicted in Figure 11, that is the tendency of early-type galaxies to have lower than average X/O values and the opposite behavior in late-type ones. As seen in Figure 13, all morphological groups, including compact objects, tend to follow the same relation. For compact objects we obtained similar parameters using S-K statistics: a correlation coefficient of ~ 0.5 and a correlation significance level $>99\%$. A least squares fit gives to the anticorrelation a slope of -2.4 and a log X/O-intercept of -0.95. Comparing different nuclear types, we found that both BLAGN and NLAGN follow the same distribution (see Figure 13). On the other hand, we did not find any clear correlation between $HR(2 - 4.5keV/0.5 - 2keV)$ and the concentration index (Figure 14), suggesting that the observed anticorrelation is not related to obscuration.

The physical origin of the observed anticorrelation is not well established. First of all, it is not easy to disentangle possible bias effects that superimposed to variable seeing conditions. It has been pointed out the existence of redshift-dependent biases in both A and C, due to the reduction of apparent size and surface brightness with respect to the sky background with increasing z, along with poorer sampling and lower S/N (Brinchmann et al. 1998; Conselice et al. 2003); on the other hand, there is a "bandpass shift" with respect to the rest wavelength (Bershady et al. 2000). Even if these effects combine to produce some uncertainty in the

⁴All fractions given here are relative to the total number of X-ray objects having optical counterpart and detected in both soft and hard2 energy bands such as $HR(2 - 4.5keV/0.5 - 2keV)$ can be computed

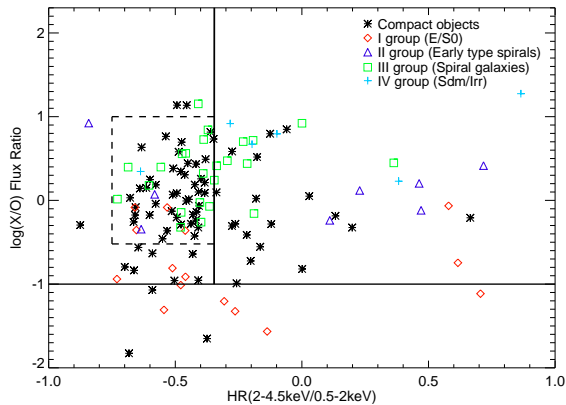


Fig. 11.— Relationship between X/O ratio and $HR(2 - 4.5keV/0.5 - 2keV)$, for the different morphological types. Solid lines separate BLAGN and NLAGN regions and the area with $X/O < 0.1$, where stars, normal galaxies and Compton thick AGNs can be found (Fiore et al. 2003). Dashed line box presents the limits obtained by Della Ceca et al. (2004) where $\sim 85\%$ of their spectroscopically identified BLAGN have been found. In our case, inside of this box can be found $\sim 51\%$ of all objects from the diagram.

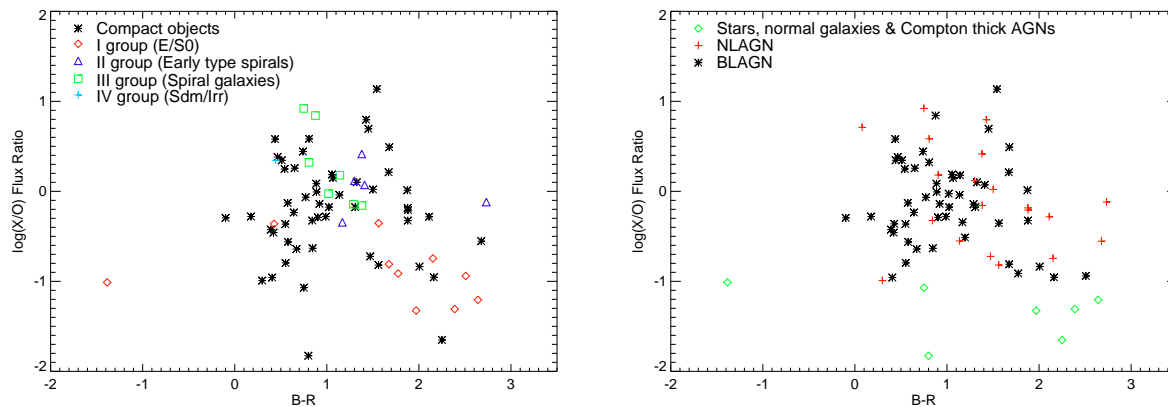


Fig. 12.— $\log(X/O)$ flux ratio vs. B-R color for different morphology (left) and nuclear types (right).

morphological classification of galaxies, generally in the sense of shifting objects to apparently later Hubble types (i.e. with lower C values), A and C seems to be reproducible out to $z = 3$, within a reasonable scatter (Conselice et al. 2003). Moreover, there can be a truly evolutionary effect in the AGN host galaxies, indicating that galaxies at higher redshift are intrinsically less concentrated (Grogin et al. 2005).

At this stage we cannot apply any correction which depends on the redshift, although this is one of the objectives for the future work. However, we have performed a preliminary evaluation

by representing the concentration index C versus the spectroscopic redshifts z gathered from the DEEP2 catalog for 84 objects from our sample. While for non compact objects we obtained an anticorrelation between these two parameters, C and z are found uncorrelated for compact objects, in clear contrast with the observed behavior in Figure 13.

So, although the biases described above might contribute partially to it, the observed anticorrelation seems to also be a result of a true physical effect. In order to attempt to explain it, we have first to understand the physical connections of the

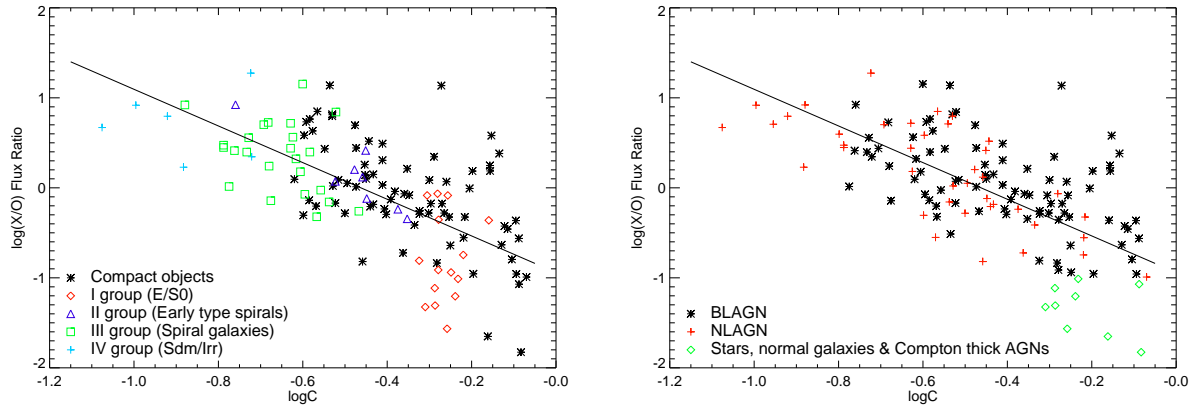


Fig. 13.— Relationship between X/O and the Abraham concentration index C for different morphological (left) and nuclear types (right). A clear anticorrelation is observed.

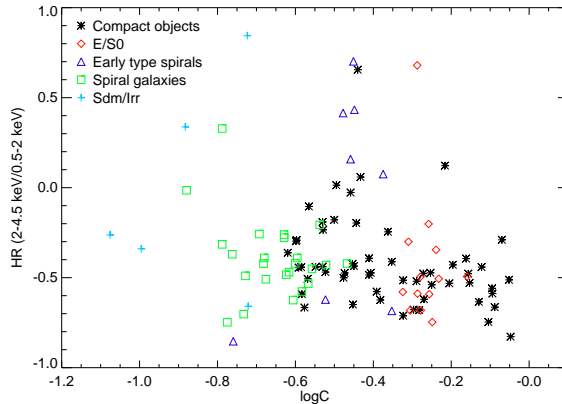


Fig. 14.— Relationship between the hardness ratio $HR(2-4.5\text{keV}/0.5-2\text{keV})$, and the concentration index C for the different morphological types.

two observables C and X/O. The concentration index (C) is tightly linearly correlated to the central velocity dispersion (Graham et al. 2001a,b), which is in turn related to the nuclear black hole (BH) mass (e.g. Magorrian et al. 1998). Therefore, the concentration and the nuclear BH mass (M_{BH}) are correlated. The physical connections of the X-ray to optical flux ratio are not so evident. The X/O ratio measures the X-ray flux (in the 0.5-4.5keV band), normalized with the R-band optical flux of the whole galaxy (nucleus, bulge and disk). It should be noted that no band-pass, or K-correction is performed; therefore if the sample spans a large redshift range the interpretation of the quantity becomes more prob-

lematic. If the nuclear luminosity is large compared with that of the host galaxy, X/O ratio can be thought as a measure of the X-ray to optical spectral index, α_{OX} ⁵. This parameter has been found to be strongly anticorrelated with the UV luminosity $L_{2500\text{\AA}}$, without a significant correlation with redshift (Steffen et al. 2006). On the other hand Bian (2005) found a strong correlation between the hard/soft X-ray spectral index, α_X and the Eddington ratio in a sample of 41 BLAGN and narrow-line Seyfert 1 (NLS1) galaxies observed with ASCA. Other works have con-

⁵This relation is usually defined as $\alpha_{OX} = 0.3838 \log(f_{2\text{keV}}/f_{2500\text{\AA}})$

firmed this correlation (Grupe 2004; Shemmer et al. 2006). The relationship between α_X and α_{OX} has not been thoroughly studied in large samples of AGN, but a linear correlation has been found between both spectral indexes in a sample comprising 22 out of 23 quasars in the complete the Palomar-Green X-ray sample with $z < 0.4$ and $M_B < -23$ (Shang et al. 2007). If this last correlation holds for our sample, X/O could be tracing the Eddington ratio in the large nuclear luminosity limit. In addition, if the host galaxy luminosity is large when compared with the nuclear luminosity ($L_{bulge+disk} \gg L_{nucleus}$), the X/O ratio can be thought as a lower bound of the X-ray-to-bulge luminosity ratio, that is in turn a (weak) measure of the AGN Eddington ratio $L/L_{Edd} \propto L/M_{BH}$, assuming that the X-ray luminosity represents the nuclear luminosity and the bulge luminosity is proportional to the bulge mass (and therefore to M_{BH}).

Hence, we can guess a (loose) correlation between X/O and the energy production efficiency of the AGN. Under these assumptions, the C vs. X/O relation traces the correlation between the Eddington ratio and the nuclear BH mass. The obtained result could therefore suggest that early-type galaxies, having poor matter supply to feed the activity, have lower Eddington rates than those of late-type, with larger reserves of the gas for AGN feeding.

This suggested approach is consistent with the results obtained by Ballo et al. (2006, 2007) in a sample of X-ray selected AGNs at $z \leq 1$. They observed that a large fraction of low-luminosity AGNs are fed by black holes with a mass $M_{BH} > 3 \times 10^6 M_\odot$, and Eddington rate $\ll 1$, while a small ($< 10\%$) fraction of AGNs host small SMBH ($M_{BH} < 10^6 M_\odot$) and Eddington rate ≈ 1 , which corresponds to a more efficient accretion rate. They stated that their results strongly suggest that most of the low-luminosity X-ray selected AGNs (at least up to $z \leq 0.8$) are powered by rather massive black holes, experiencing a low-level accretion in a gas-poor environment.

Our approach is also consistent with the results of Wu & Liu (2004), who studied the black hole masses and Eddington rates of a sample of 135 double-peaked broad line AGNs, observed in two surveys: SDSS and a survey of BLAGN ra-

dio emitters. They obtained that if the separation between the line peaks (which is correlated to the SMBH mass) decrease, the Eddington rate increases.

Kawakatu et al. (2007) found an anticorrelation between the mass of a SMBH and the luminosity ratio of infrared to active galactic nuclei Eddington luminosity, L_{IR}/L_{Edd} , for a sample of ultraluminous infrared galaxies with type 1 Seyfert nuclei (type 1 ULIRGs) and nearby QSOs, which also could be consistent with our approach. The anticorrelation is interpreted as a link between the mass of a SMBH and the rate of mass accretion onto a SMBH, normalized by the AGN Eddington rate, which indicates that the growth of the black hole is determined by the external mass supply process, and not the AGN Eddington-limited mechanism, changing its mass accretion rate from super-Eddington to sub-Eddington.

5. The clustering of X-Ray emitters and extended optical counterparts

The study of large-scale environmental conditions of AGN host galaxies are useful not only for understanding the differential properties of the AGN phenomena, but to trace the formation and evolution of such galaxies and the structures where they reside. Despite the relevance of X-ray selected AGNs, their clustering properties still remain quite unknown (Basilakos et al. 2005, and references therein). In this sense, and taking into account the characteristics of the X-ray source catalog presented in this work, we have calculated the 2-point angular correlation function (2p-ACF) for significant subsamples.

The 2p-ACF, $\omega(\theta)$, gives the excess of probability, with respect to a random homogeneous distribution, of finding two sources in the solid angles $d\Omega_1$ and $d\Omega_2$ separated by an angle θ , and it is defined as

$$dP = \mathcal{N}^2 [1 + \omega(\theta)] d\Omega_1 d\Omega_2 \quad (4)$$

where \mathcal{N} is the mean number density of cataloged sources. To measure the 2p-ACF we have follow the same procedure as done in Cepa et al. (2008), adopting the estimator of Landy & Szalay (1993), which can be written in the form

$$\omega(\theta_i) = \frac{DD - 2DR + RR}{RR} \quad (5)$$

where $DD = N_{ss}(\theta_i)$ is the fraction of possible *source-source* pairs counted in i -bins over the angular range studied and $DR = \left[\frac{(N_g-1)}{2N_r} \right] N_{gr}(\theta_i)$, $RR = \left[\frac{N_s(N_s-1)}{N_r(N_r-1)} \right] N_{rr}(\theta_i)$ are the normalized counts of *source-random* and *random-random* pairs in these bins, respectively. To make the random catalogs we placed $(200 \times N_{source})$ random points by following the X-ray source angular distribution. However, the source density is affected by several instrumental biases such as detector gaps and sensitivity variations due to survey regions with different exposure times. To account for these effects, we made normalized sensitivity maps from the effective exposure time and source distributions for each band used in this section (soft and hard2). The raw maps were modelled using a minimum-curvature algorithm. Next, the uniform density random catalogs were convolved with the corresponding sensitivity map to obtain differential number counts in the surveyed area. In the case of the HR(2–4.5keV/0.5–2keV) catalog, we adopt the sensitivity map used for the hard2 source one. The smoothed footprint of each sensitivity map can be seen in Figure 15.

We measure $\omega(\theta_i)$ in i -logarithmic bins of width $\Delta(\log \theta) = 0.2$ in the angular scales $0.24 \leq \theta \leq 24.0$ arcmin. The lower limit in angular separation is according to the minimum detection scale defined in the Section 2.1.2. The formal error associated with the 2p-ACF measured is the Poissonian estimate $\sigma_\omega^2 = \frac{1+\omega(\theta_i)}{DD}$. The 2p-ACF binned measures were fitted using the $A_\omega(\theta^{1-\gamma} - C)$ power law. We adopted a fixed canonical slope $\gamma=1.8$ (the so called “comoving clustering model”) and C is defined as

$$C = \frac{\sum N_{rr}(\theta) \theta^{-0.8}}{\sum N_{rr}(\theta)} \quad (6)$$

corresponding to the numerical estimation of the “integral constraint” (Peebles 1980). As in Miyaji et al. (2007), we use the normalization A as the fitting parameter rather than the correlation length $\theta_c = A^{1/(\gamma-1)}$, since the former gives better convergence of the fit.

From the whole catalog we have selected the soft (0.5–2 keV) and hard2 (2–4.5 keV) sources (given their similar depths in the survey), the X-ray objects with $HR(2 - 4.5keV/0.5 - 2keV) \neq 0$ and the fraction of X-ray sources with optical

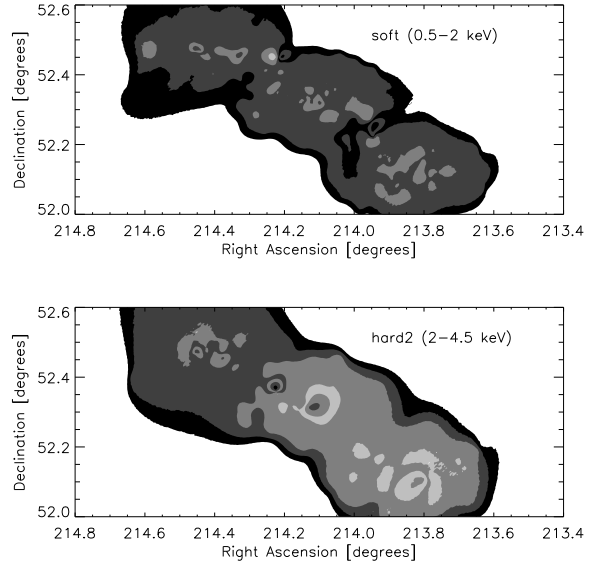


Fig. 15.— Smoothed sensitivity maps in the soft (0.5–2 keV) and hard2 (2–4.5 keV) bands, used to convolve the uniform density random catalogs. The sensitivity dimension is normalized to the maximum exposure time in each band. Contours are linearly binned and lighter regions correspond to higher sensitivities.

counterparts. Table 2 summarizes the basic results of the correlation analysis for these subsamples. In all cases, we have obtained significant positive clustering signal. Regarding the soft band sample, the correlation length θ_c derived from A_ω is consistent with the obtained by Basilakos et al. (2005) (XMM-Newton LSS) and it is $\sim 2\sigma$ larger than the values obtained by Gandhi et al. (2006), Carrera et al. (2007) and Ueda et al. (2008). In the specific case of the hard2 band, we only found in the literature the 2p-ACF estimations of Miyaji et al. (2007), valid for X-ray sources detected in the XMM-Newton observations of the COSMOS field and corresponding to their MED band: our fitted correlation length is ~ 4.3 times larger, although our sample is a factor 2 deeper.

In Figure 16 are represented our 2p-ACF measurements with the best-fit $A_\omega \theta^{-0.8}$ power-law in soft and hard2 bands (panels a and b, respectively). It is noticeable that the clustering amplitude obtained in both bands looks similar. Thus, in the case of the Groth field, we would not expect

Table 2: Clustering properties of the X-ray selected sources. N_{source} is the number of data points used in the 2p-ACF estimation and A_ω is the best-fit value in the separation range given by $\theta_{\min} - \theta_{\max}$, assuming a power-law $\omega(\theta) = A_\omega \theta^{(1-\gamma)=-0.8}$. The goodness-of-fit statistics (χ^2) and the fitted 2p-ACF at 1 arcmin [$\omega(1')$] are given in the final columns. The errors represent 1σ uncertainties.

Subsample	N_{source}	$\theta_{\min} - \theta_{\max}$ arcmin	A_ω ($1 - \gamma = -0.8$) $\times 10^{-3}$ degrees	χ^2	$\omega(1')$
soft (0.5-2 keV)	465	0.24-24.0	6.99 ± 0.68	0.030	0.15 ± 0.02
hard2 (2-4.5 keV)	266	0.24-24.0	9.19 ± 1.28	0.107	0.20 ± 0.03
HR _(2-4.5keV/0.5-2keV)	190	0.24-24.0	9.68 ± 1.30	0.109	0.21 ± 0.03
Optical counterparts ($I \leq 23$)	104	0.60-24.0	19.99 ± 3.32	0.096	0.42 ± 0.07

redshift or spatial clustering differential effects in the soft and hard2 band samples. Interestingly, an absence of correlation in differently defined hard bands has been reported by Gandhi et al. (2006) and Puccetti et al. (2006); nevertheless, Yang et al. (2003) and Basilakos et al. (2004) not only yield a positive correlation amplitude, but the hard band signal is several times that of the soft band. Other results with similar correlation lengths in both bands are given by Carrera et al. (2007), Miyaji et al. (2007) and Yang et al. (2006).

In the panel c of Figure 16 is represented the 2p-ACF estimations for a HR(2-4.5keV/0.5-2keV) selected sample. The clustering amplitude is slightly larger than the soft or hard2 band ones. Moreover, the whole HR(2-4.5keV/0.5-2keV) subsample was decomposed using the boundary referred in Sect. 4.1 to separate type 1 (or BLAGN) from type 2 (or NLAGN) populations and a positive, very similar clustering signal from both subsamples emerged from the 2p-ACF estimations, despite their goodness-of-fit statistics are worse than the tabulated values in a factor ~ 1 because of the small size of the subsamples.

Finally, we measured the 2p-ACF of the optical counterparts of X-ray sources in order to compare the clustering behavior with those that come from the analysis of galaxy populations in the same field. For a reliable comparison is necessary to diskard the compact objects (i.e. with CLASS_STAR > 0.9) from the optical counterparts catalog, as well as all objects fainter than a limiting magnitude. We have selected the peak of the apparent brightness distribution in the I-band as such limiting magnitude. Thus, X-ray coun-

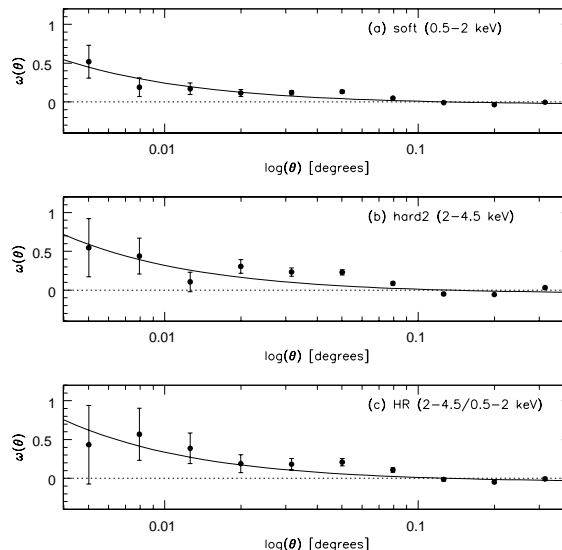


Fig. 16. — 2p-ACF estimates of the X-ray sources detected in the soft band (panel a), hard2 band (panel b) and HR as defined in eq. 1 (panel c). The continuous line represents the $A_\omega \theta^{(1-\gamma)=-0.8}$ power law fit to the data.

terparts with $I > 23$ were ruled out, remaining 104 extended objects, which can be regarded as AGN host candidates of the corresponding X-ray sources.

In spite of this skinny sample, it is possible to obtain some interesting lines of thought about the X-ray selected AGN clustering. It is suggested that the typical environments of AGNs are no different to those of inactive galaxies in general, at

redshift ranges above $z \sim 0.4$ (e.g. Grogin et al. 2003; Waskett et al. 2005). Nevertheless, Coil et al. (2004) and Gilli et al. (2005) have argued that the AGN are preferentially hosted by early-type galaxies at a typical redshift of ~ 1 . In this way, Basilakos et al. (2004) found that clustering length values of hard X-ray objects are comparable with those of Extremely Red Objects (EROs) and luminous radio sources. More recently, Georgakakis et al. (2007) demonstrated that X-ray-selected AGNs at $z \sim 1$, in the AEGIS field, avoids underdense regions at 99.89% of significance.

In Figure 17 we have depicted the 2p-ACF of the optical counterparts selected as described above. The 2p-ACFs of the Groth field galaxy sample with $I \leq 23$ only and with $V-I > 3$ ($I \leq 24$) from Cepa et al. (2008) are overplotted. At least in the range $0.01 \leq \theta \leq 0.1$ degrees, the clustering signal produced by the optical counterparts of our X-ray sources is $1-2\sigma$ stronger than the corresponding to the $I \leq 23$ galaxy population. In terms of fitted correlation length, the $\theta_c(\text{X-ray})$ ($1-\gamma = -0.8$) is ~ 30 times larger than that of the Groth field galaxies, but only ~ 2.3 times larger than the maximum correlation length of the $V-I > 3$ galaxies in the same field. In the other hand, using the optical data from the counterparts catalog, we found that the median $V-I$ observed color is 1.86 and most of 65% of the optical counterparts have an observed color $V-I > 2$. This means that a significant population of our optical counterparts is a composition of red and very red galaxies, whereas its clustering signal tends to reproduce that associated with such galaxies, which drive the $\sim 10x$ clustering excess found by Cepa et al. (2008). At once, more than a 55% of the optical counterparts belong to the morphological categories I and II, as defined in the Section 3.2.1.

6. Summary and Conclusions

We processed and analyzed public, 200 ksec *Chandra*/ACIS observations of three fields comprising the original GWS gathered from the *Chandra* Data Archive, combined with our broadband survey carried out with the 4.2m WHT at La Palma. Our X-ray catalog contains 639 unique X-ray emitters, with a limit flux at 3σ level of $4.8 \times 10^{-16} \text{ erg cm}^{-2} \text{ s}^{-1}$ and a median flux of $1.81 \times 10^{-15} \text{ erg cm}^{-2} \text{ s}^{-1}$ in the full (0.5-7 keV) band.

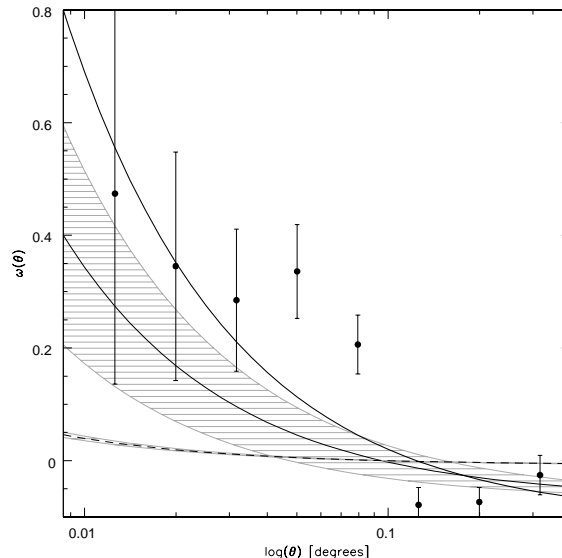


Fig. 17.— 2p-ACF estimation for the optical extended ($\text{CLASS_STAR} \leq 0.9$) counterparts with I magnitude brighter than 23 (solid circles). The continuous thick line represents the $A_w \theta^{(1-\gamma)=-0.8}$ power law fit to the data. The dashed line represents the 2p-ACF estimation for galaxies with $I \leq 23$ in the Groth field, whereas the continuous thin line it does for the $V-I > 3$ color selected galaxies with $I \leq 24$, both extracted from Cepa et al. (2008). The shaded regions represent fitting errors of 1σ .

Cross-matching the X-ray catalog with our optical broadband catalog, we have found 340 X-ray emitters with optical counterparts. The completeness and the reliability of cross-matching procedure are 97% and 88.9%, respectively. At our flux limit, the number counts of our complete X-ray sample are in good agreement with Nandra et al. (2005) and other comparison surveys mentioned in Section 3.1. X-ray SEDs of the majority of our sources are compatible with the power law model, affected with the galactic absorption column density and the intrinsic absorption. We have performed a morphological classification obtaining and analyzing different structural parameters, including the bulge-to-total ratio, residual parameter, Sérsic index, asymmetry and concentration indexes. We also performed the classification based on visual inspection. To obtain the nu-

clear classification, we applied a criterium based on the correlation between X/O flux ratio and HR1' hardness ratio. 63% of our sources, with HR1' $\neq 0$, have been classified as BLAGNs. The electronic table summarizes the X/O flux ratios, HR1' values and morphological classification of all 340 X-ray emitters with optical counterparts. We have investigated the correlations between X-ray and broadband optical structural parameters that provide with information about the host galaxy morphology and populations, finding that:

1. For a sample where most of the objects are faint ($R \geq 22$) and with small isophotal area (≤ 300 pixels), bulge-to-total flux ratio has revealed inaccurate to perform the morphological classification. Concentration index combined with the asymmetry index have been found to provide the best separation criterion for such a sample. different morphological types have been observed to distribute according to the following ranges of concentration index: group 0 (compact objects) $\rightarrow C \geq 0.7$ (or CLASS_STAR ≥ 0.9), group I (E, E/S0 and S0) $\rightarrow 0.45 \leq C < 0.7$, group II (S0/S0a-Sa) $\rightarrow 0.3 \leq C \leq 0.45$ (0.47), group III (Sab-Scd) $\rightarrow 0.15 \leq C \leq 0.3$ and group IV (Sdm-Irr) $\rightarrow C \leq 0.15$

2. No clear separation has been found between the morphology and the nuclear type, but most of our objects classified as compact are placed in the region of BLAGNs.

3. We can confirm the tendency of compact and late type objects to show bluer colors, while early type galaxies tend to present redder colors. On the other hand, we find a mild tendency of BLAGNs to show bluer colors when compared with NLAGNs.

4. We obtained an anticorrelation between the X-to-optical flux ratio and the concentration index (which parametrizes the morphology), with significance level higher than 99%, showing that the early-type galaxies tend to have lower and the late-type galaxies higher than average X/O values. Objects classified as compact show this anticorrelation as well, with the same significance level. The anticorrelation might suggest that early-type galaxies, having poor matter supply to feed the activity, have lower accretion rates than those of late type, with larger reserves of gas for AGN feeding.

Finally, we presented the first results on the two-point angular correlation function of the X-ray selected sources in the Groth field from *Chandra*/ACIS observations, segregated in four sub-

samples: soft, hard2, HR $_{(2-4.5keV/0.5-2keV)}$ and optical extended counterparts. We obtain the following results and conclusions:

1. All subsamples reveal a significant positive clustering signal in the ~ 0.5 to 6 arcmin separation regime. Canonical power-law ($\gamma=1.8$) fits to the angular correlation functions have been made, obtaining correlation lengths between ~ 7 and 27 arcsec, depending on the subsample.

2. We have neither found substantial differences between the clustering of soft and hard2 selected X-ray sources, nor when comparing the populations of type 1 and type 2 AGN (i.e. 'unobscured' and 'obscured' AGN, respectively), separated using the HR $_{(2-4.5keV/0.5-2keV)} \approx -0.35$ boundary.

3. The clustering analysis of the optical counterparts of our X-ray emitters provides a correlation length significantly larger than the one found for the whole galaxy population with the same limiting magnitude, and same field, but similar to that of strongly clustered populations like red and very red (bulge-dominated) galaxies. A clustering signal $> 1\sigma$ was observed even at $\theta \sim 30$ arcsec, which corresponds to $160 h^{-1}$ kpc, assuming a mean redshift of 0.85 for *Chandra* extragalactic sources (Hasan 2007). This comoving distance is, for instance, comparable to the separation of two mergers in the $t \approx 2$ Gyr stage of their large-scale evolution, according to the model of Mayer et al. (2007) on rapid formation of SMBH. Hence, our results suggest that the environment plays an important (but not unique) role as possible triggering mechanism of AGN phenomena. This fact can be perfectly compatible with the interpretation given to the anticorrelation between X/O ratio and the concentration index. The former may be associated to the genesis of the AGNs, while the anticorrelation could be that to their maintenance and evolution.

7. Acknowledgements

This work was supported by the Spanish *Plan Nacional de Astronomía y Astrofísica* under grants AYA2005-04149 and AYA2006-2358. JIGS and JGM acknowledge financial support from the Spanish Ministerio de Educación y Ciencia under grants AYA2005-00055 and AYA2006-2358,

respectively.

This research has made use of software provided by the Chandra X-ray Center (CXC) in the application packages CIAO and ChIPS.

IRAF is distributed by the National Optical Astronomy Observatory, which is operated by the Association of Universities for Research in Astronomy (AURA) under cooperative agreement with the National Science Foundation.

This publication makes use of data products from the Two Micron All Sky Survey, which is a joint project of the University of Massachusetts and the Infrared Processing and Analysis Center California Institute of Technology, funded by the National Aeronautics and Space Administration and the National Science Foundation.

We would like to thank Laura Tomás who kindly provided us with her software for diagnosis of hardness ratios using model grids.

We acknowledge support from the Faculty of the European Space Astronomy Centre (ESAC).

REFERENCES

- Abraham, R. G., van der Bergh, S., Glazebrook, K., Ellis, R. S., Santiago, B. X. & Surma, P. 1996, *ApJ*, 107, 1
- Abraham, R. G., Valdes, F., Yee, H. K. C., & van der Bergh, S. 1994, *ApJ*, 432, 90
- Alexander, D. M., Brandt, W. N., Hornschemeier, A. E., Garmire, G. P., Schneider, D. P., Bauer, F. E., & Griffiths, R. E. 2001, *AJ*, 122, 2156
- Alexander, D. M., Bauer, F. E., Brandt, W. N., Garmire, G. P., Hornschemeier, A. E., Schneider, D. P., & Vignali, C. 2003, *Astronomische Nachrichten*, 324, 8
- Arnaud, K. A. 1996, *ASPC*, 101, 17
- Ballo, L., Cristiani, S., Fasano, G., Fontanot, F., Monaco, P., Nonino, M., Pignatelli, E., Tozzi, P., Vanzella, E., Fontana, A., Giallongo, E., Grazian, A., & Danese, L. 2007, *ApJ*, 667, 97
- Ballo, L., et al. 2006, *Proceedings of the The X-ray Universe 2006 (ESA SP-604)*, ESA-SP.604..595B
- Barcons, X. et al. 2007, *A&A*, 476, 1191
- Barger, A. J., et al. 2003, *AJ*, 126, 632
- Basilakos, S., Georgakakis, A., Plionis, M., & Georgantopoulos, I. 2004, *ApJ*, 607, L79
- Basilakos, S., Plionis, M., Georgakakis, A., & Georgantopoulos, I. 2005, *MNRAS*, 356, 183
- Bershady, M. A., Jangren, A. & Conselice, C. J., 2000, *AJ*, 119, 2645
- Bertin, E. & Arnouts, S. 1996, *A&AS*, 117, 393
- Bian, W. H., 2005, *A&AS*, 5, 289
- Brandt, W. N., & Hasinger, G. 2005, *ARA&A*, 43, 827
- Brinchmann, J., Abraham, R., Schade, D., Tresse, L., Ellis, R. S., Lilly, S., Le Fèvre, O., Glazebrook, K., Hammer, F., Colless, M., Crampton, D., Broadhurst, T., 1998, *ApJ*, 499, 112
- Cappelluti, N., et al. 2007, *ApJS*, 172, 341
- Capak, P. et al. 2007, *ApJS*, 172, 99
- Carrera, F. J., et al. 2007, *A&A*, 469, 27
- Cepa, J., Pérez García, A. M., Bongiovanni, A., Alfaro, E., Castañeda, H. O., Gallego, J., González-Serrano, J. I., Sánchez-Portal, M., González, J. J. 2008, *A&A*, 490, 1
- Cepa, J., Alfaro, E. J., Bland-Hawthorn, J., Castañeda, H. O., Gallego, J., González-Serrano, J. I., González, J. J., Jones, D. Heath, Pérez-García, A. M., Sánchez-Portal, M. 2005, *Rev. Mexicana Astron. Astrofis.*, 24, 82
- Coil, A. L., Newman, J. A., Kaiser, N., Davis, M., Ma, Ch., Kocevski, D. D., Koo, D. C. 2004, *ApJ*, 617, 765
- Conselice, C. J., 2003, *ApJS*, 147, 1
- de Ruiter, H. R., Willis, A. G. & Arp, H. C. 1977, *A&AS*, 28, 211
- Della Ceca, R., Maccacaro, T., Caccianiga, A., Severgnini, P., Braito, V., Barcons, X., Carrera, F. J., Watson, M. G., Tedds, J. A., Brunner, H. & 4 coauthors 2004, *A&A*, 428, 383
- Dickinson, M. et al. 2004, *ApJ*, 99, 122
- Ferrarese, L. & Merritt, D. 2000, *ApJ*, 539, L9

- Fiore, F., Elvis, M., Maiolino, R., Nicastro, F., Siemiginowska, A., Stratta, G., & D'Elia, V. 2003, *A&A*, 409, 57
- Fiore, F., Antonelli, L. A., Ciliegi, P., Comastri, A., Giommi, P., La Franca, F., Maiolino, R., Matt, G., Molendi, S., Perola, G. C., Vignali, C. 2001, *AIPC*, 599, 111
- Furusawa, H., et al. 2008, *ApJS*, 176, 1
- Gandhi, P., et al. 2006, *A&A*, 457, 393
- Gebhardt, K. et al. 2000, *ApJ*, 119, 1157
- Georgakakis, A. et al. 2006, *MNRAS*, 371, 221
- Georgakakis, A., et al. 2007, *ApJ*, 660, L15
- Giacconi, R., et al. 2002, *ApJS*, 139, 369
- Gilli, R., et al. 2003, *ApJ*, 592, 721
- Gilli, R., et al. 2005, *A&A*, 430, 811
- Graham, A. W., Trujillo, I., & Caon, N. 2001a, *AJ*, 122, 1707
- Graham, A., Erwin, P., Caon, N. & Trujillo, I 2001b, *ApJ*, 563, L11
- Grogin, N. A., et al. 2003, *ApJ*, 595, 685
- Grogin, N. A., et al. 2005, *ApJ*, 627, L97
- Grupe, D., 2004, *AJ*, 127, 1799
- Hasan, P. 2007, *Ap&SS*, 312, 63
- Im, M., Simard, L., Faber, S. M., Koo, D. C., Gebhardt, K., Willmer, C. N. A., Phillips, A., Illingworth, G., Vogt, N. P., & Sarajedini, V. L. 2002, *ApJ*, 571, 171
- Kauffmann, G. et al. 2003, *MNRAS*, 346, 1055
- Kawakatu, N. et al. 2007, *ApJ*, 661, 660
- Laird, E.S., et al. 2008, *ApJS*, *submitted*
- Landy, S. D. & Szalay, A. S. 1993, *ApJ*, 412, 64
- Magorrian, J., et al. 1998, *AJ*, 115, 2285
- Manners, J. C., et al. 2003, *MNRAS*, 343, 293
- Mayer, L., Kazantzidis, S., Madau, P., Colpi, M., Quinn, T. & Wadsley, J. 2007, *Science*, 316, 1874
- Miyaji, T., et al. 2007, *ApJS*, 172, 396
- Mushotzky, R. 2004, *Supermassive Black Holes in the Distant Universe*, 308, 53
- Nandra, K., et al. 2005, *MNRAS*, 356, 568
- Peebles, P. J. E. 1980, *The Large Scale Structure of the Universe* (Princeton University Press)
- Puccetti, S., et al. 2006, *A&A*, 457, 501
- Sánchez-Portal, M., Díaz, A. I., Terlevich, E., & Terlevich, R. 2004, *MNRAS*, 350, 1087
- Sánchez-Portal, M., Pérez García, A. M., Cepa, J., González-Serrano, J. I., Alfaro, E. J., Castañeda, H. O., Gallego, J., González, J. J 2007, *Rev. Mexicana Astron. Astrofis.*, 29, 175
- Schade, D., Lilly, S. J., Le Fevre, O., Hammer, F. & Crampton, D. 1996, *ApJ*, 464, 79S
- Schade, D., Lilly, S. J., Crampton, D., Hammer, F., Le Fevre, O. & Tresse, L. 1995, *ApJ*, 451, 1
- Shang, Z., Wills, B. J., Wills, D. & Brotherton, M. S., 2007, *AJ*, 134, 294S
- Shemmer, O., Brandt, W. N., Netzer, H., Maiolino, R., Kaspi, S. 2006, *ApJ*, 646, 29
- Simard, L., Willmer, C. N. A., Vogt, N. P., Sarajedini, V. L., Phillips, A. C., Weiner, B. J., Koo, D. C., Im, M., Illingworth, G. D., & Faber, S. M. 2002, *ApJS*, 142, 1S
- Simard, L. 1998, *ASPC*, 145, 108
- Steffen, A.T., Strateva, I., Brandt, N., Alexander, D. M., Koekemoer, A. M., Lehmer, B. D., Schneider, D. P. & Vignali, C., 2006, *AJ*, 131, 2826
- Stetson, P. B. 1987, *PASP*, 99, 191
- Taylor, M. B. 2005, *ASPC*, 347, 29
- Ueda, Y., et al. 2008, *ArXiv e-prints*, 806, arXiv:0806.2846
- Waskett, T. J., Eales, S. A., Gear, W. K., McCracken, H. J., Lilly, S., & Brodwin, M. 2005, *MNRAS*, 363, 801
- Wu, X. & Liu, F. K. 2004, *ApJ*, 614, 91

Yang, Y., Mushotzky, R. F., Barger, A. J., Cowie,
L. L., Sanders, D. B., & Steffen, A. T. 2003,
ApJ, 585, L85

Yang, Y., Mushotzky, R. F., Barger, A. J. &
Cowie, L. L. 2006, ApJ, 645, 68

Yee, H. K. 1983, ApJ, 272, 473